

# 1 Resilience to sensory variance in the primary visual 2 cortex

3 Hugo J Ladret<sup>1,2,\*</sup>, Nelson Cortes<sup>2</sup>, Lamyae Ikan<sup>2</sup>, Frédéric Chavane<sup>1</sup>, Christian  
4 Casanova<sup>2</sup>, and Laurent U Perrinet<sup>1</sup>

5 <sup>1</sup>Institut de Neurosciences de la Timone, UMR 7289, CNRS and Aix-Marseille Université, Marseille, 13005, France

6 <sup>2</sup>School of Optometry, Université de Montréal, Montréal, QC H3C 3J7, Canada

7 \*Corresponding author : hugo.ladret@univ-amu.fr

## 8 ABSTRACT

9 Our daily endeavors occur in a complex visual environment, whose intrinsic variability is fundamental to the way we integrate  
information to make decisions. By processing myriads of parallel sensory inputs, our brain is theoretically able to compute the  
variance of its environment, a cue which is known to guide our behavior. Yet, the neurobiological and computational basis of  
such variance computations are still poorly understood. Here, we quantified sensory variance modulations of primary visual  
cortex neurons, both in orientation tuning and in dynamics. We report two archetypal responses, one of which is resilient to  
changes in variance and can co-encode the sensory feature and its variance, significantly improving the population encoding of  
orientation. The existence of these variance-specific responses could be accounted for by a model of intracortical recurrent  
connectivity, which furthers our understanding of how the brain performs computations on complex, naturalistic inputs.

## 10 Introduction

11 Selectivity to the orientation of visual stimuli is an archetypal feature of neurons in the mammalian primary visual cortex (V1)<sup>1</sup>.  
12 This filter-like property of V1 neurons has been historically described using low-complexity artificial stimuli, such as oriented  
13 gratings<sup>2</sup>. These artificial stimuli offer a clear hypothesis as to what neurons are responding to, but only probe for neural  
14 correlates of single parameters in V1 (orientation, spatial frequency, ...), which constitutes an experimental limit to our  
15 understanding of the rich cortical dynamics involved in natural vision<sup>3</sup>, which are driven not only by these local parameters, but  
16 also by a global context<sup>4</sup>. In orientation space, this means that most of our fundamental knowledge of V1 is currently based on  
17 responses to single orientations, rather than more naturalistic responses to many simultaneous orientations.

18 This knowledge gap is not trivial, since the variance between the oriented elements of natural images is a fundamental cue  
19 on which our brain relies to produce coherent integration of sensory inputs and prior knowledge of the world<sup>5,6</sup> in order to  
20 drive behaviour<sup>7</sup>. Bayesian inference rules would even posit that low-variance inputs are processed through fast feedforward  
21 pathways, whereas higher sensory variance relies on a slower, recurrent integration<sup>8</sup>. How the brain performs computations on  
22 variance, however, is still a relatively unexplored terrain. V1 recordings have shown that single neurons undergo non-linear  
23 tuning modulations as a function of their input's variance<sup>9</sup> which can be used as a functional encoding scheme<sup>10,11</sup>. These  
24 results are well accounted for by historical models of recurrent cortical activity of V1<sup>12,13</sup> and match psychophysical metrics of  
25 human subjects<sup>14–16</sup>. While local intra-V1 interactions are sufficient to encode orientation variance<sup>17</sup>, the quantification of  
26 single neuron responses and their link to a population encoding of variance remains to be established.

27 Here, we used stimuli which match the orientation content of natural images<sup>18</sup> to study the neural basis of variance processes  
28 in V1. We provide a quantitative description of the variance/tuning relationship of single neurons, both in terms of orientation  
29 selectivity and dynamical modulation, which falls into two archetypal responses to variance. We report that some neurons are  
30 endowed with a degree of invariance to sensory variance, remaining well tuned to orientation even at very high levels of sensory  
31 variance. We show that only these "resilient neurons" are performing a co-encoding of both orientation and variance, improving  
32 the overall encoding of orientation distributions in V1. A well-established model of intracortical V1 recurrence can account for  
33 the presence of these neurons, which matches their predominant locations within supragranular cortical layers. This fits notably  
34 well with canonical Bayesian frameworks<sup>6</sup>, potentially establishing uncertainty computations as a new general role for local  
35 recurrent cortical connectivity.

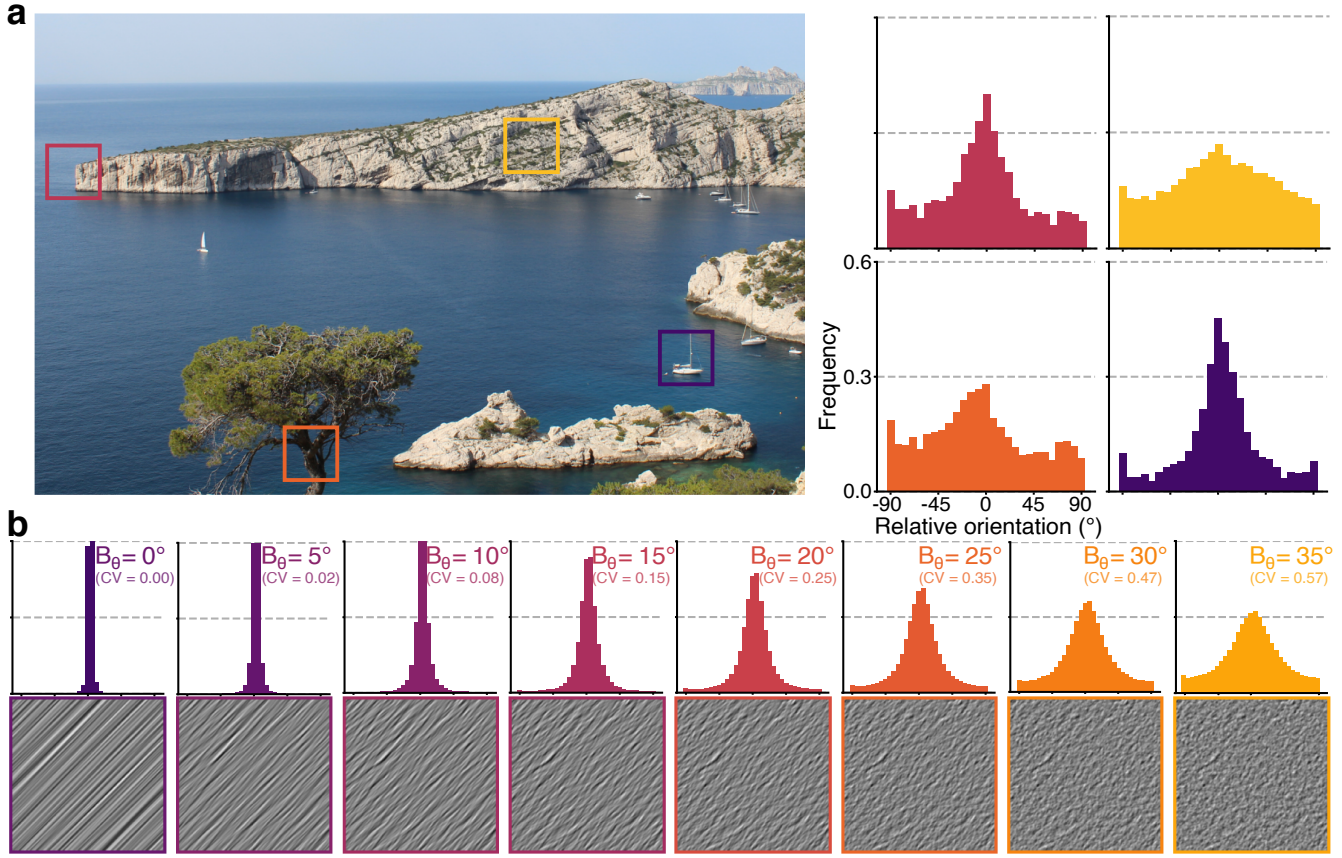


**Figure 1.** Variance of the orientation distributions characterizes local regions of natural images. **(a)** Distributions of orientation retrieved from four local regions of a natural image (picture taken by H.J.L) using an histogram of oriented gradients (32x32 pixels per cell, 200x200 pixels per region), centered around the most frequent orientation. **(b)** Motion Clouds, naturalistic stimuli (bottom row) oriented at an angle  $\theta = 45^\circ$  relative to the horizontal axis, with increasing variance  $B_\theta$  from left to right. Distributions of orientation retrieved from the stimuli (as done with the natural image) are shown on the upper row. Circular Variance (CV) of the distribution is shown to compare  $B_\theta$  with a common orientation metric.

## 36 Results

### 37 Single neuron response in V1 depends on input variance

38 We recorded neural activity from 249 neurons in anesthetized cat V1, and measured orientation-selective response to naturalistic  
 39 images called Motion Clouds<sup>18</sup>. These stimuli are band-pass filtered white noise textures that have three major advantages over  
 40 both simple grating-like stimuli and complex natural images. First, they rely on a generative framework, which here allows to  
 41 finely control both the mean  $\theta$  and the variance  $B_\theta$  of the orientation distribution in a stimulus, thereby closely reproducing  
 42 the oriented content of natural images (Figure 1). Second, they are stationary in the spatial domain and thus only probe the  
 43 orientation space, which removes any potential second-order information found in natural images which could be exploited  
 44 by the visual cortex<sup>19</sup>. Third, they conform to the statistics of natural images, namely the  $1/f^2$  distribution of the power  
 45 spectrum<sup>20</sup>, which gives them an overall ideal compromise between controllability and naturalness<sup>21</sup>. Here, 96 Motion Clouds  
 46 were generated by varying the mean orientation  $\theta$  between 0 and  $180^\circ$  in 12 even steps and the variance  $B_\theta$  between  $\approx 0^\circ$  and  
 47  $35^\circ$  in 8 evenly spaced steps.

48 All neurons showed orientation selectivity to Motion Clouds, and almost all of them kept responding to their same preferred  
 49 orientation when variance  $B_\theta$  was increased (98.8% units,  $p < 0.05$ , Wilcoxon signed-rank test) while markedly diminishing  
 50 in peak amplitude of tuning curve (95.1% units,  $p < 0.05$ , Wilcoxon signed-rank test, 73.1% mean amplitude decrease for  
 51  $B_\theta = 36^\circ$ ), such that only 28.5% of the recorded units were still tuned for  $B_\theta = 35.0^\circ$  stimuli ( $p < 0.05$ , Wilcoxon signed-rank  
 52 test). Increments of input variance thus decrease single neuron tuning, which unfolded heterogeneously across neurons, as  
 53 evidenced by two representative single units shown in Figure 2a. Neuron A is an example of a single unit which is no longer  
 54 orientation-tuned when variance  $B_\theta$  reaches  $35^\circ$  ( $W = 171.0$ ,  $p = 0.24$ , Wilcoxon signed-rank test), contrarily to neuron  
 55 B ( $W = 22.5$ ,  $p = 10^{-6}$ ) which exemplifies the aforementioned 28.5% of variance-resilient units. Both types of responses

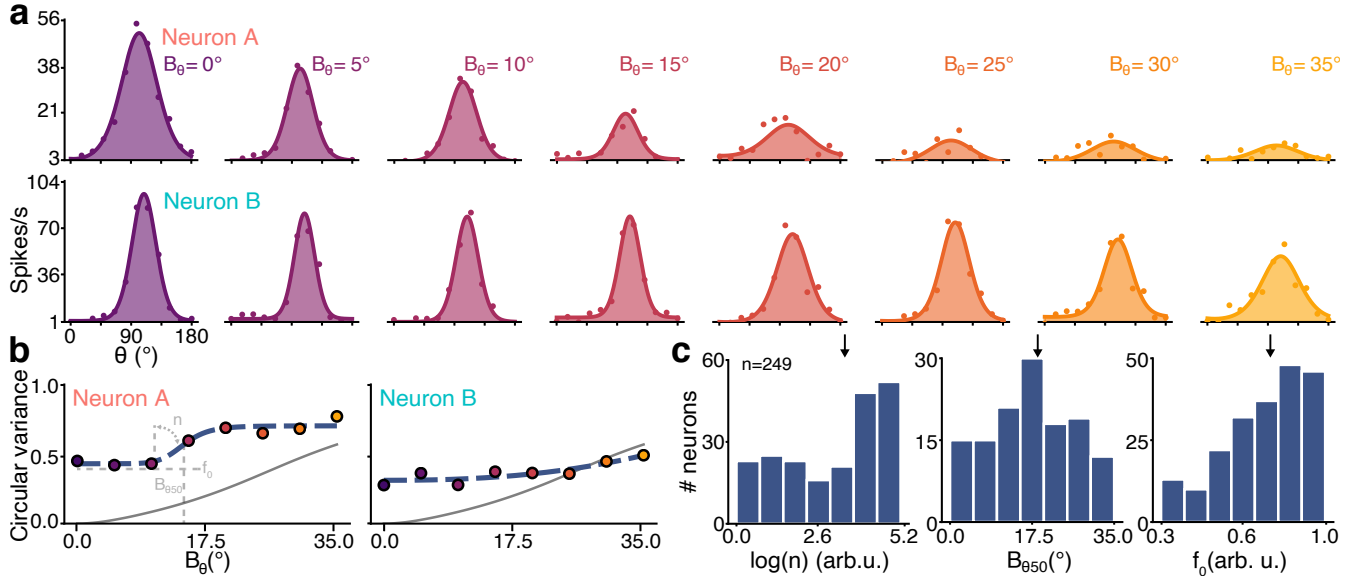


**Figure 2.** Single neuron tuning correlates with input variance to V1. Additional examples are provided in Figure S 1.

(a) Tuning curves of two example neurons responding to Motion Clouds of increasing variance  $B_\theta$  from left to right. Dots represent the mean firing rate across trials (baseline subtracted, 300 ms average) and lines a fitted von Mises function.  
 (b) Variance-tuning functions (VTF), assessing the change of orientation tuning measured by the circular variance (CV, dots) as a function of variance  $B_\theta$ , fitted with a Naka-Rushton (NKR) function (dashed curves, parameters shown in light gray). Parameters of the VTF are  $\log(n) = 8.4$ ,  $B_{\theta50} = 14.7^\circ$ ,  $f_0 = 0.4$  for neuron A and  $\log(n) = 2.4$ ,  $B_{\theta50} = 35.0^\circ$ ,  $f_0 = 0.3$  for neuron B. The CV identity curve is shown in solid gray. (c) Histograms of the NKR parameters (in the [5%;95%] range of possible NKR fitting values) for the 249 recorded units. Median values are indicated by a black arrow ( $\log(n) = 3.6$ ,  $B_{\theta50} = 19.2^\circ$ ,  $f_0 = 0.75$ ).

are further characterized by their  $B_\theta$  to goodness of tuning (circular variance, CV) relationships. Such "variance-tuning functions" (VTF, Figure 2b) define an input/output ratio of variance in orientation space and were well fitted by a Naka-Rushton function<sup>22</sup> (Figure S 2) and summarized the response to changes of sensory variance with three parameters:  $n$ , the degree of non-linearity of the VTF ;  $B_{\theta50}$ , the level of input variance at which a neuron's response transitioned from tuned to untuned state (i.e. the changepoint) and  $f_0$ , the goodness of orientation tuning for inputs with the lowest variance. We also measured variance-bandwidth and variance-response functions (see supfig) which showed XXX These VTF revealed an heterogeneous response to variance between V1 neurons, with median values describing a prototypical VTF that is slightly non-linear with a changepoint at  $B_\theta = 19.2^\circ$  (Figure 2c).

Orientation variance impacts not only orientation tuning, but also the dynamics of the response of V1 neurons (Figure 3). Interestingly, both effects are linked, as shown by the two example VTFs : example neuron B, which produced orientation-tuned responses for  $B_\theta = 35^\circ$  inputs (Figure 2a), exhibited slower time-dependant change of goodness of tuning (relative min. of reduction of 42% of max. CV at 200 ms post-stimulation onset,  $B_\theta = 0^\circ$ ) compared to neuron A (relative min. of 26% of max. CV at 90 ms post-stimulation onset, Figure 3b). These dynamical modulations were also heterogeneously distributed in the population, significantly more spikes emitted 200 ms after stimulation onset for  $B_\theta = 35^\circ$  (Figure 3d,  $U = 14936.0$ ,  $p < 0.001$ , Mann-Whitney U-test). Overall, orientation variance creates changes in both tuning and dynamics of V1 neurons with seemingly two archetypal types of response : either fast in time and non-linear with respect to variance (neuron A) or slow in time with linear changes of orientation tuning when variance increases (neuron B).

### Multiple types of variance responses are found in V1

To properly characterize the two aforementioned types of responses to variance, we separated the recorded neurons in two groups, by K-means clustering the Principal Components (PC, Figure 4) of the neuronal responses. Rather than raw data, we performed clustering on the VTFs (Figure 4b), the statistical measurements of tuning (Figure 4c,d) and on the dynamics of response (Figure 4e,f). We used the first 2 PC for separating the data, which accounted for 39.1% of cumulative variance (Figure S 4a), and chose two clusters for the K-means algorithm, both with regard to the number of example responses shown before and due to the empirical absence of an "elbow"<sup>23</sup> in the Within-Clusters-Sum-of-Squares (WCSS) curve, which, when present, is typically used to select the number of clusters (Figure S 4b). This split the data into a cluster of 164 neurons, to which

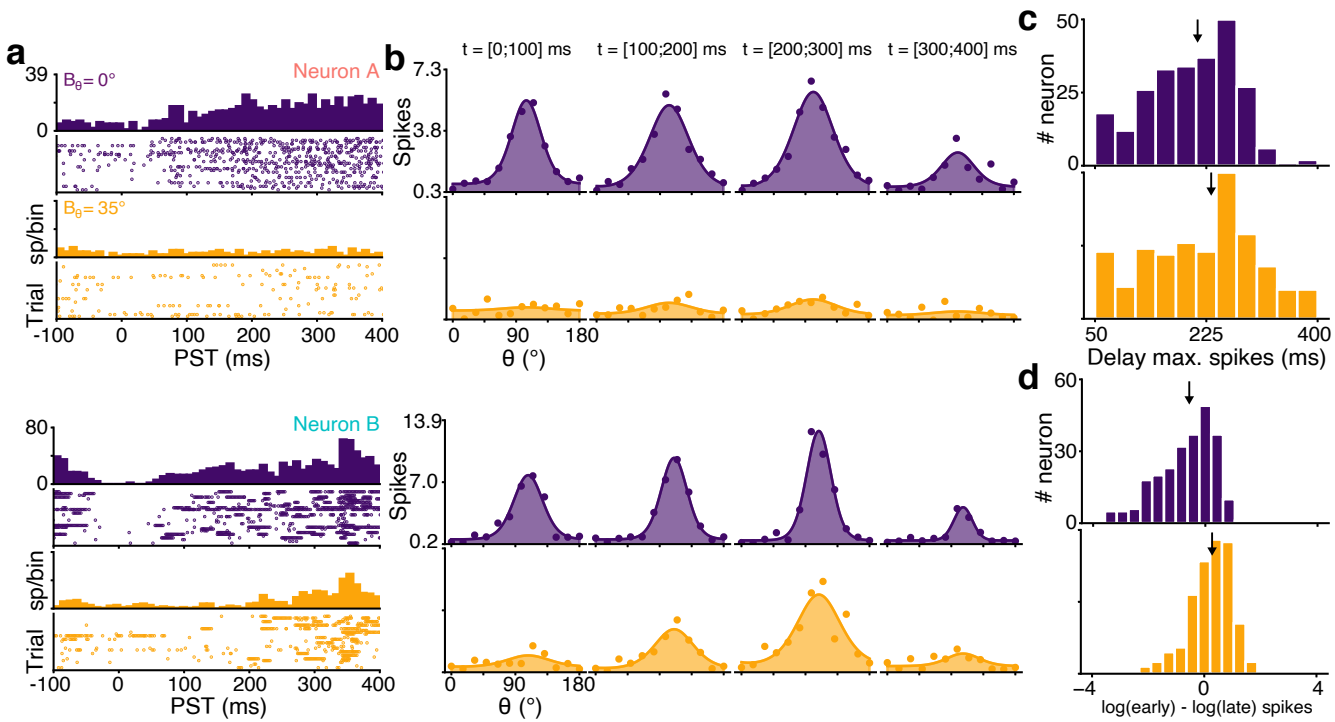


**Figure 3.** Dynamics of orientation response depend on input variance to V1. Additional examples are provided in Figure S 3. **(a)** Peristimulus time (PST) histogram and associated rasterplot of the two previous example neurons, for input variance  $B_\theta = 0^\circ$  (purple) and  $B_\theta = 35^\circ$  (yellow). **(b)** Dynamics of the tuning curves in 100 ms windows, starting at the time labelled atop of each column. **(c)** Delay to maximum peak amplitude of tuning curves for  $B_\theta = 0^\circ$  (purple, median = 210 ms) and  $B_\theta = 35^\circ$  (yellow, median = 233 ms) for the whole population. Median values are indicated by a black arrow. **(d)** Log ratio of early (< 100 ms post-stimulation) and late (> 200 ms) spike counts for  $B_\theta = 0^\circ$  (median = -0.54) and  $B_\theta = 35^\circ$  (median = 0.27) for the whole population.

belonged neuron A, whilst the rest of the data (85 neurons) was associated with the response types of neuron B. Given how this neuron displayed resilience to increase of input variance (Figure 2a), its cluster was labelled "resilient neurons". Conversely, the neurons clustered with neuron A were designated as "vulnerable neurons" (blue and red colors, respectively, Figure 4a).

The K-means clustering created a significant difference between the two groups' VTF parameters (Figure 4b) : resilient neurons had significantly more linear modulations ( $\log(n)$ ,  $U = 4029.0.0$ ,  $p < 0.001$ , Mann-Whitney U-test), higher change-points ( $B_{\theta50}$ ,  $U = 7854.0$ ,  $p = 0.028$ ) and better tuning to low-variance inputs ( $f_0$ ,  $U = 4992.0$ ,  $p < 0.001$ ), which endows them with the ability to respond to orientation on a wider range of input variance<sup>24,25</sup>. This is coherent with the clustering on the statistical measurement of orientation tuning, which showed that resilient neurons were still significantly tuned to higher values of  $B_\theta$  ( $B_{\theta max}$ , Figure 4c,  $U = 9155.0$ ,  $p < 0.001$ ). However, when  $B_\theta$  reached 35°, both groups of neurons had similar circular variance (Figure 4d). Taken together, this indicates that both types of neurons were similarly poorly tuned for inputs of highest variance, but underwent difference tuning changes between  $B_\theta = 0^\circ$  and  $B_\theta = 35^\circ$ . In terms of dynamics, the two groups exhibited the same differences that characterized neuron A and B. Resilient neurons discharged significantly later than vulnerable neurons for  $B_\theta = 0^\circ$  (Figure 4e,  $U = 8455.5$ ,  $p = 0.002$ ), but both group were on par for inputs of  $B_\theta = 35^\circ$  ( $U = 7794.5$ ,  $p = 0.063$ ). Surprisingly, the time to maximum amplitude of the tuning curve was significantly lower in resilient neurons for  $B_\theta = 0^\circ$  (Figure 4f,  $U = 5542.5$ ,  $p = 0.014$ ), which is the inverse of the early/late ratio of spikes. Neither group showed variance-dependent modulation of the delay to maximum spike ( $U = 3058.0$ ,  $p = 0.084$  and  $U = 11545.5$ ,  $p = 0.090$  for resilient and vulnerable, respectively), and both group had similar delay for  $B_\theta = 35^\circ$  ( $U = 6094.5$ ,  $p = 0.158$ ).

The existence of these two groups of neurons could not be explained by an integration of the drifting motion of the stimuli (direction selectivity index, Figure 4g,  $U = 7031.5$ ,  $p = 0.910$ ). Rather, the location of the recorded units (unused in the clustering process) predominantly placed the resilient neurons in supragranular layers, which could provide a mechanistic basis for their existence (Figure 4h). Further, these neurons had sharper orientation tuning and slower dynamics, which are distinctive features of supragranular neurons<sup>26,27</sup>. This, however, does not assign a functional role to these two types of responses in V1.

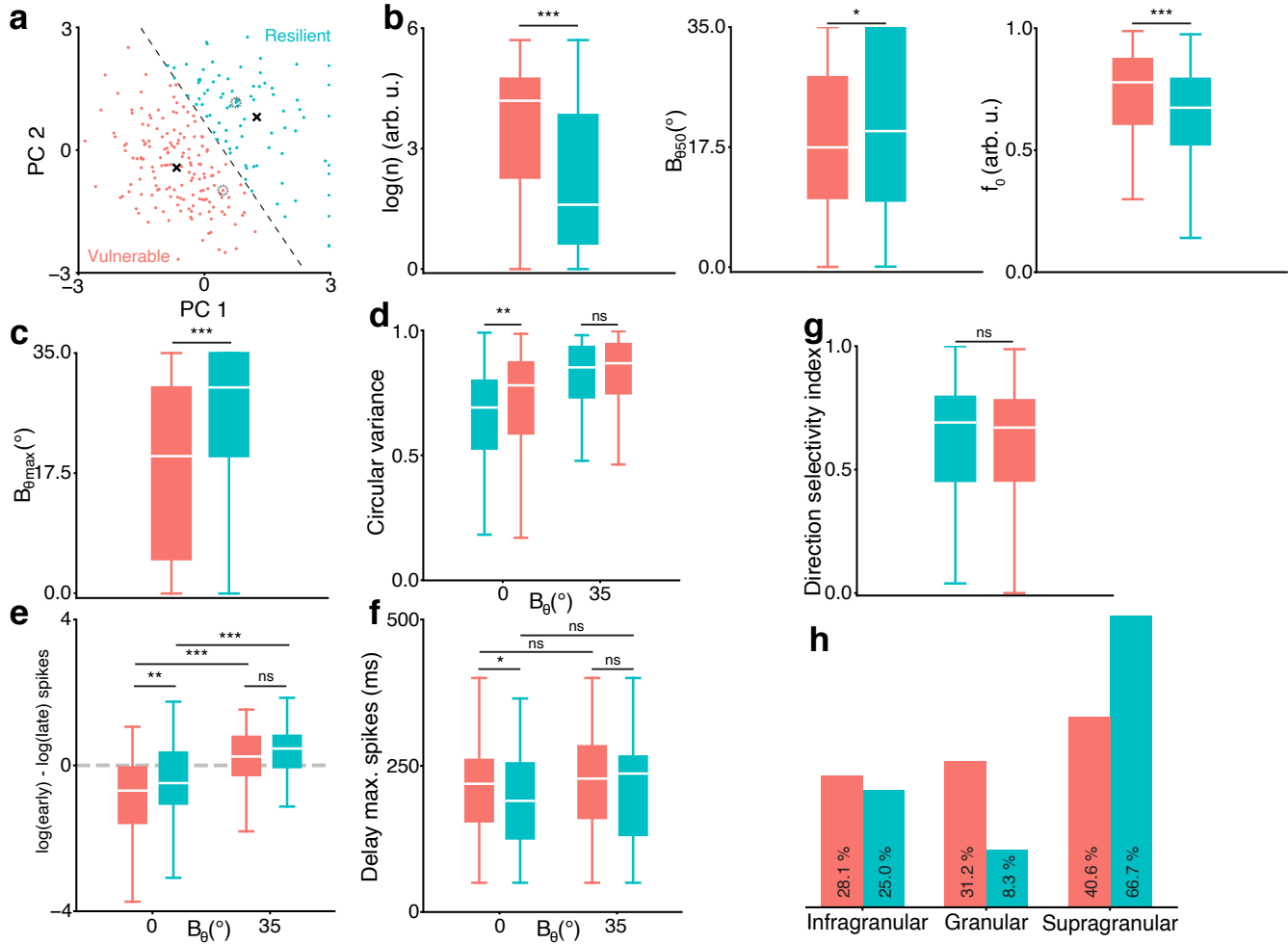


**Figure 4.** Responses to changes in variance fall into two categories. (a) Principal Components (PC) analysis of the data, K-Means clustered in two groups (2 clusters, centroids shown as black crosses and separatrix as dashed line). 9 resilient neurons with PC1 larger than 3 are plotted at PC1 = 3. Neuron A and B are shown as dashed circles. (b) Boxplot of the VTF parameters  $\log(n)$ ,  $B_{\theta 50}$ ,  $f_0$  (ns, not significant; \*,  $p < 0.05$ ; \*\*,  $p < 0.01$ , \*\*\*,  $p < 0.001$  Mann-Whitney U-test). (c) Maximum  $B_\theta$  at which a neuron yields a significant orientation tuning curve. (d) Circular variance for  $B_\theta = 0^\circ$  and  $B_\theta = 35^\circ$ . (e) Log ratio of the early ( $< 100$  ms) and late ( $> 200$  ms) spike counts for  $B_\theta = 0^\circ$  and  $B_\theta = 35^\circ$ . (f) Delay to the maximum peak amplitude of tuning curves for  $B_\theta = 0^\circ$  and  $B_\theta = 35^\circ$ . (g) Direction selectivity index of the two groups (unused in the clustering). (h) Laminar position of the two groups (unused in the clustering).

### Population level modulations of the orientation code

To understand the functional role played by resilient and vulnerable neurons, we used a neuronal decoder that probes for population codes in V1, which allowed understanding of what parameters of the stimuli each neuron group is encoding. We trained a multinomial logistic regression classifier<sup>28</sup>, a probabilistic model that classifies data belonging to multiple classes (see Methods). This classifier was given the firing rate of neurons in a sliding time window (100 ms) and learned, for each neuron, a coefficient that best predict the class (i.e. the generative parameter  $\theta, B_\theta$  or  $\theta \times B_\theta$ ) of the stimulus.

We used this decoder to probe for representation of the stimuli's orientations  $\theta$  in the population activity. For this purpose, the dataset of trials was separated for each variance, such that 8 independent,  $B_\theta$ -specific, orientation decoders were learned, with optimal parametrization (Figure S 5). These orientation decoders were able to retrieve the correct stimulus'  $\theta$  well above the chance level (1 out of 12 orientations, max. accuracy = 10.56 and 4.68 times chance level for  $B_\theta = 0^\circ$  and  $B_\theta = 35^\circ$ , respectively) from the entire population recordings. The temporal evolution of the accuracy of these decoders (Figure 5a) showed that maximally accurate orientation encoding correlates almost linearly with the stimuli's variance (Figure 5e, black). As the decoders are trained independently in each time window, this accumulative process occurs in the recordings themselves, rather than in the decoding algorithm.

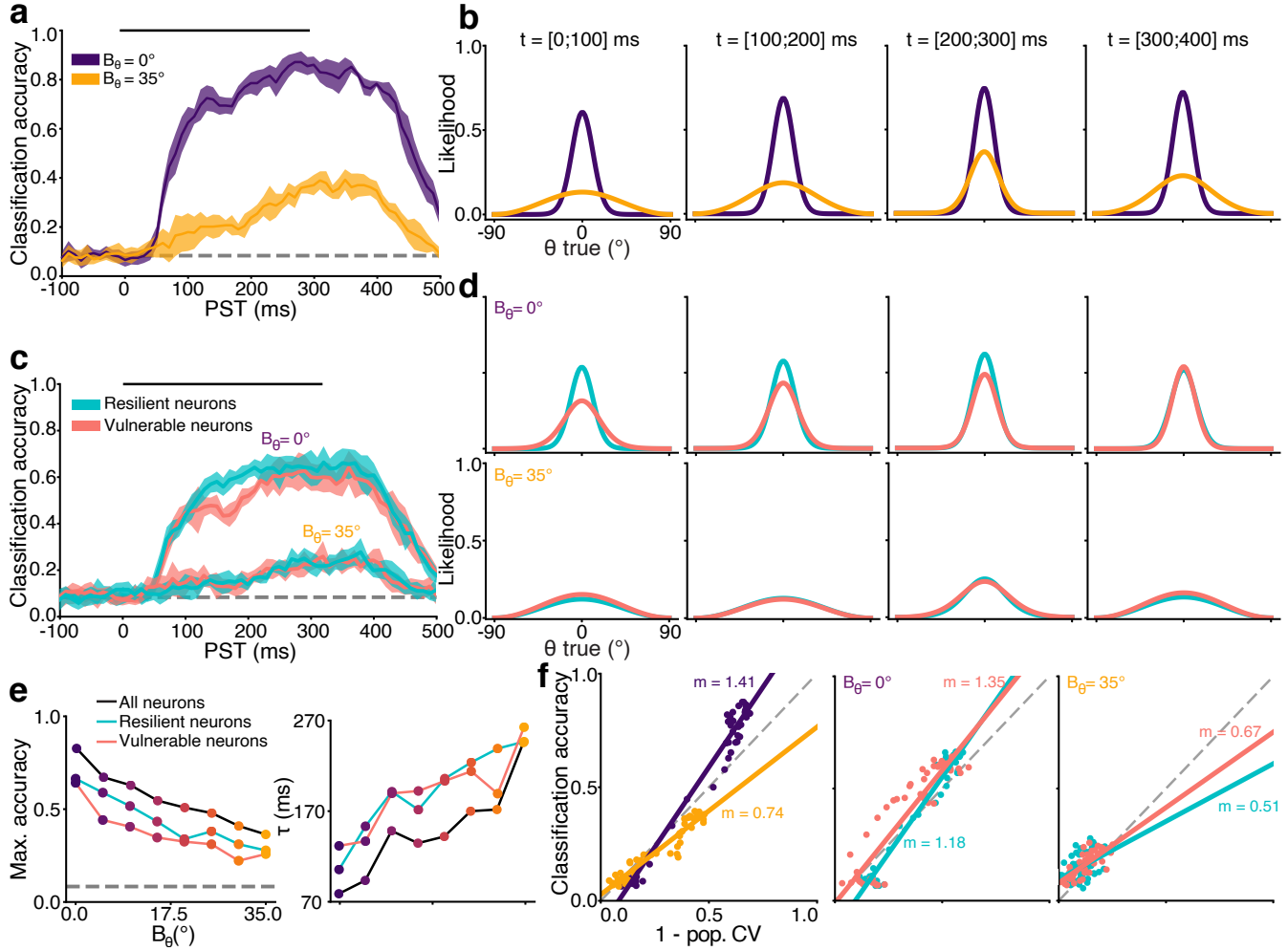


**Figure 5.** Input variance modulates orientation encoding in V1. (a) Time course of the accuracy for decoding orientation  $\theta$  at two variances  $B_\theta$ . Lines are the mean accuracy of a 5-fold cross validation and contour the STD. Decoding at chance level is represented by a gray dashed line and stimulation time by a black line. (b) Population tuning curves fitted with a von Mises function, showing the likelihood of decoding each  $\theta$  in four time windows, centered around the correct  $\theta$ . (c) Same as Figure 5a for the two groups of neurons. (d) Same as Figure 5b for the two groups of neurons, with  $B_\theta = 0^\circ$  on the upper row and  $B_\theta = 35^\circ$  on the lower row. (e) Parameters of the decoding time course the three decoders at all  $B_\theta$ , estimated by fitting a sigmoid to decoding time course up to PST = 300 ms, where  $\tau$  is the time constant. (f) Correlation between classification accuracy and population circular variance for the whole population (left), for both groups with  $B_\theta = 0^\circ$  (middle) and  $B_\theta = 35^\circ$  (right). Linear regression are shown as solid lines with slope  $m$  indicated (all significant,  $p < 0.001$ , Wald Test with t-distribution).

117 The full output of these decoders (see Methods) is a population tuning curve, which shows the likelihood of decoding all  
 118 possible input classes (here, all  $\theta$ , Figure 5b), rather than just the proportion of correct decoding reported by the accuracy metric.  
 119 The clear correlation between the sharpness of these population tuning curves (Figure 5f left) and the accuracy of the decoder  
 120 shows that improvements of decoding accuracy rely directly on a population-level separation of features within orientation  
 121 space<sup>28</sup>, and even more so at higher  $B_\theta$  (Figure 5b, third panel). Overall,  $B_\theta$  modulates the dynamics of the orientation code in  
 122 V1. The short delay required to process precise inputs is congruent with the feedforward processing latency of V1<sup>29</sup>, while  
 123 the increased time required to reach maximum accuracy for low precision oriented inputs hints at the presence of a slower,  
 124 recurrent, mechanism.

125 We then sought to assert the role of the vulnerable and the resilient neural populations by decoding  $\theta$  from either group.  
 126 The number of neurons in each group was imbalanced (79 more vulnerable neurons), which influences the accuracy of the  
 127 decoder (Figure S 5), and we thus removed iteratively vulnerable neurons who had the least effect on maximum accuracy  
 128 until both groups had the same number of neurons. This resulted in an overall reduction of only 1.5% maximum accuracy

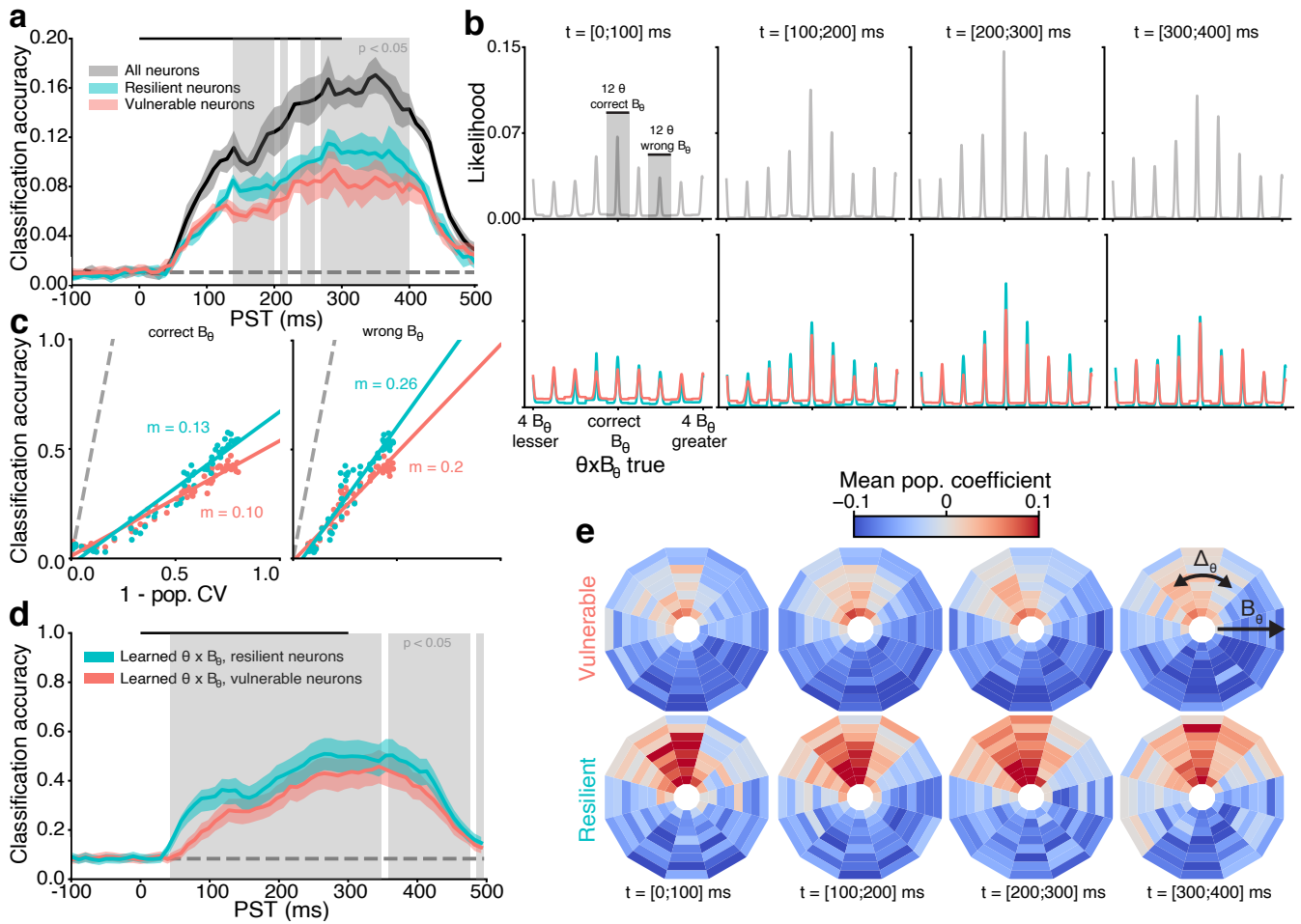


**Figure 6.** Resilient neurons encode both orientation and its variance. (a) Time course of the accuracy for decoding both the orientation and variance  $\theta \times B_\theta$  of Motion Clouds. The solid dark line represents the mean accuracy of a 5-fold cross validation and the filled contour the SD. Significantly better decoding from resilient over vulnerable neurons is indicated as a grey overlay (1000 permutations test,  $n=6$  cross validations, threshold  $p < 0.05$ ). Decoding at chance level (here, 1/96) is represented by the gray dashed line. (b) Population tuning curves, showing the likelihood of decoding each  $\theta \times B_\theta$  in four time windows, centered around the correct  $\theta \times B_\theta$ . Each of the 8  $B_\theta$ -specific tuning curve is fitted with an independent von Mises function. (c) Correlation between classification accuracy and population circular variance for correct  $B_\theta$  population tuning curves (left) and averaged across other  $B_\theta$  tuning curves curves (right). Linear regression are shown as solid lines with slope  $m$  indicated (all significant  $p < 0.001$ , Wald Test with t-distribution). (d) Time course of the  $\theta \times B_\theta$  decoder, marginalized over  $B_\theta$  to produce  $\theta$ -only outputs. (e) Mean decoding coefficients of the two groups yielded from the whole population  $\theta \times B_\theta$  decoder.

for the vulnerable group, which is thus an upper estimation of this group's decoding capacity. Using the same approach as with the global population decoding, we then trained  $B_\theta$ -specific orientation decoders on the activity of either group of neurons. The overall decoding performance of both groups were similar (Figure 5c), with identical time courses but slightly (non-significant) better overall accuracy for resilient neurons (Figure 5e). Despite the better tuning of resilient neurons to inputs with higher variance (Figure 4), both groups have overall similar orientation encoding performances, even at  $B_\theta = 35^\circ$ . Interestingly, the population tuning curves (Figure 5d) reveal that resilient neurons have sharper population tuning curves when  $B_\theta = 35^\circ$  (Figure 5f, right), but neither groups do not seem to have a different functional role in encoding orientation at the population level.

#### 137 A subset of V1 neurons co-encode orientation and its variance

Given that orientation encoding did not account for a difference in functional roles of resilient and vulnerable neurons, we then probed for an encoding of the other parameter of stimulus generation, the variance  $B_\theta$ . The same type of decoder previously used failed to infer the variance  $B_\theta$  (chance level = 1 out of  $8B_\theta$ , max. accuracy = 1.91 times chance level) of the stimuli from

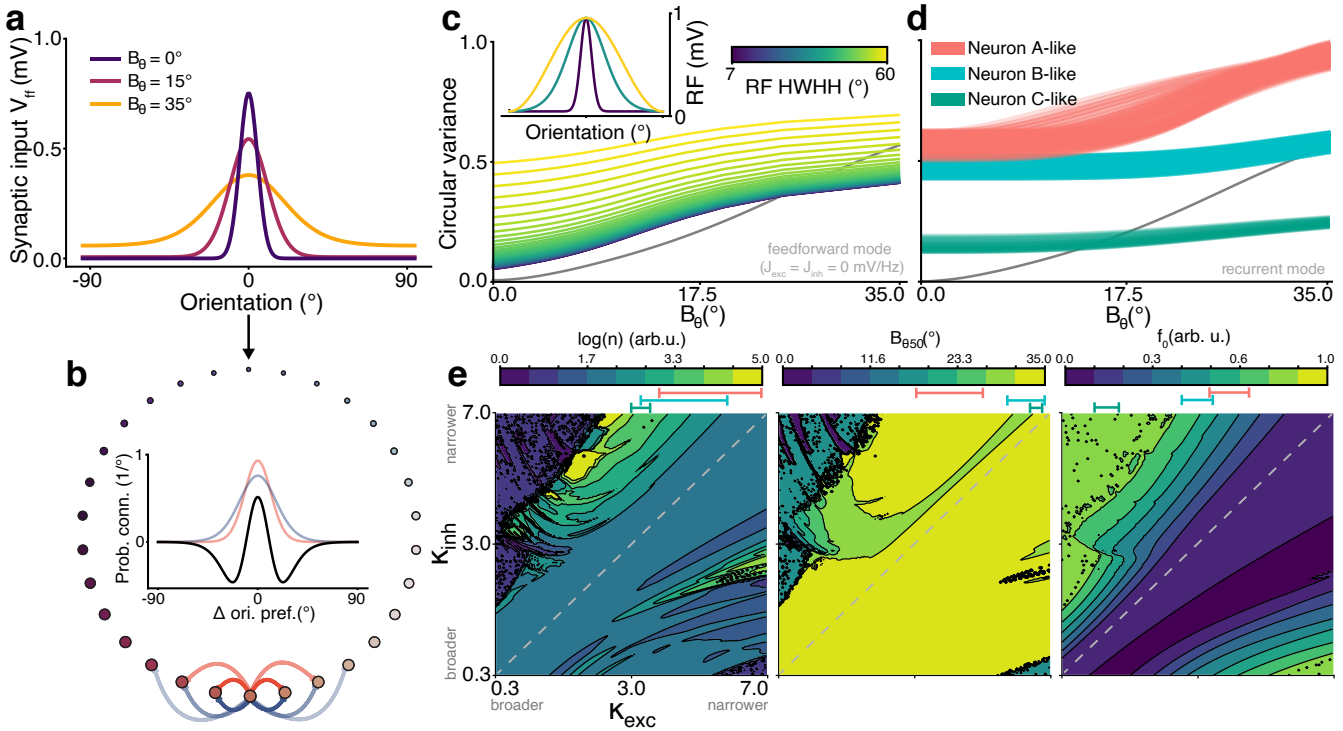


**Figure 7.** A model of recurrent interaction can explain the existence of resilient and vulnerable neurons. **(a)** Feedforward inputs  $V_{ff}$  to the neurons tiling the  $[-90^\circ; 90^\circ]$  orientation space, for three values of  $B_\theta$ . **(b)** Neurons are arranged in a ring topology, dictating the preferred orientation of each neuron. Inset : Recurrent connectivity profile for each neuron, computed as a difference (black) of excitatory (red) and inhibitory (blue) profiles, controlled by a measure of concentration  $\kappa_{exc}$  and  $\kappa_{inh}$ , respectively. **(c)** VTF of the model without recurrent connectivity (i.e. only inputs convolved with receptive fields) and with varying RF's Half-Width at Half-Height (HWHH). The CV identity curve is shown in black. Inset shows examples of receptive fields RF. **(d)** VTF of the model with recurrent connectivity, under two configurations retrieved by searching for VTF parameters close to those of neuron A, B (Figure 2b) and C (Figure S 1). **(e)** VTF parameters obtained from the model for each connectivity profile, shown as a contour plot of  $\kappa_{exc}$  and  $\kappa_{inh}$ . [5%;95%] range of the parameters of the VTFs shown in Figure 7 are displayed below the scale bars.

the population activity (Figure S 7a,b). At the single neuron scale, tuning curves flatten with increments of variance (Figure S 2a), which makes it hard to distinguish activity at the orthogonal orientation with  $B_\theta = 0.0^\circ$  from the activity at the preferred orientation with  $B_\theta = 35.0^\circ$ . This variance decoding also failed to reach more than twice the chance level (max. accuracy = 1.72 and 1.71 times chance level for resilient and vulnerable neurons, respectively) in both resilient and vulnerable neurons (Figure S 7c,d). Thus, neither the encoding of variance  $B_\theta$  nor the encoding of orientation  $\theta$  accounts for a different role between resilient and vulnerable neurons.

Rather than assuming that V1 is an encoder of single parameter of a stimulus, a more realistic assumption is to think of the visual system's natural inputs as distribution of information (Figure 1) from which cortical neurons must process contexts over thalamic inputs<sup>30</sup>, as part of a probabilistic-based computational principle<sup>31</sup>. Here, this means that the natural form of processing for a V1 neuron would co-encoding both the mean feature ( $\theta$ ) and its associated variance ( $B_\theta$ ).

We thus trained a  $\theta \times B_\theta$  decoder, i.e. a decoder that retrieves both orientation and variance of the stimulus' simultaneously. This decoder correctly predicted orientation and variance with a maximum accuracy reaching 16.36 times the chance level (1/96, Figure 6a, gray). The particular likelihood structure (Figure 6b, upper row) showed that the correct  $\theta$  was decoded with many concurrent hypothesis over  $B_\theta$ . The progressive increase of accuracy stems from the emergence of a dominant encoding of  $\theta$  at the correct  $B_\theta$ , which reduces the relative magnitude of representations over other  $B_\theta$  as time elapses. Interestingly, resilient neurons showed here a significantly different functional role from vulnerable neurons, with markedly better co-encoding of  $B_\theta$  and  $\theta$  (max. accuracy = 11.0 and 9.0 times chance level for resilient and vulnerable neurons, respectively, Figure 6a, blue, red). Both groups had similar ambiguity on  $B_\theta$  (Figure 6b, lower row), and similar sharpening/accuracy ratios on the correct  $B_\theta$  population curve (Figure 6c, left) or on the off-median population curves (Figure 6c, right).

To understand the usefulness of this co-encoding, we marginalized the decoder over  $B_\theta$ , creating an orientation-only

encoder which learned both orientation and variance. Data from resilient neurons then provided significantly better encoding of orientation than vulnerable neurons (max. accuracy = 6.0 and 5.4 times the 1/12 chance level for resilient and vulnerable neurons respectively, Figure 6d, gray regions), demonstrating that the overall V1 orientation code improves when co-encoding variance. The difference between resilient and vulnerable neurons is further established by the decoder coefficients, which represent the contributions of each type of neurons towards the overall  $\theta \times B_\theta$  code (Figure 6e, for single neuron examples see Figure S 8). Here, these coefficients are represented in the form a polar plot, where the error of the orientation classification  $\Delta_\theta$  is shown as the angle of each bin from the upper vertical and the variance  $B_\theta$  is representing as the eccentricity of each bin from the center. Visualizing the coefficients of the whole population decoder (trained on the 249 neurons, Figure 6a, gray) shows that the output learned from resilient neurons co-informs about both orientation and variance, as observed by the extent of the bins in the eccentricity ( $B_\theta$ ) axis (Figure 6c, bottom row). Conversely, the decoding process yielded an orientation-only information from the activity of vulnerable neurons (Figure 6c, top row). Although the coefficients are learned independently at each time steps, the difference of information between the two groups of neurons is extremely stable through time.

Resilient neurons can thus co-encode both orientation and its variance simultaneously, while vulnerable neurons can only encode orientation. Given this functional difference between the two groups of neurons, we finally address the question of how both types of neurons can exist in V1.

## Recurrent activity can explain the existence of neurons co-encoding orientation and variance

One difference between vulnerable and resilient neurons is their different location within the cortical layers (Figure 4h). This typically implies differences in local circuitry, particularly in the intra-V1 recurrent interactions between cortical columns that are mostly confined to supragranular layers<sup>32</sup>. Given that resilient neurons are predominantly found in these supragranular layers, we sought a mechanistic explanation for the existence of the two groups of neurons based on local interactions in V1. We derived a novel model from a well-established computational model of recurrent connectivity in V1, which was first used to account for the intracortical activity in cat V1<sup>33</sup> and later simplified as a center-surround filter in the orientation domain<sup>27</sup>. This model has already accounted for a wide range of emerging properties in cortical circuits<sup>34,35</sup>. Briefly, this model is built of orientation selective neurons tiling the orientation space and connected amongst themselves via recurrent synapses which follow an excitatory/inhibitory difference of von Mises distributions (Figure 7b). Here, we model inputs with higher variance as more spread in orientation space (Figure 1) and thus in model space (Figure 7a), which hence drives the recurrent dynamics of the model based on  $B_\theta$  (for a full description, see Methods).

Given that feedforward connectivity with heterogeneous tuning can encode mixtures of orientations and natural images<sup>9</sup>, we first ran our model without recurrent synapses. We reproduced the heterogeneous selectivity by convolving the input with tuning curves of varying bandwidths (Figure 7d, inset). This feedforward mode of the network was only able to produce a limited number of responses (Figure 7d), in which increasing the bandwidth of the tuning curves increased the parameter  $f_0$  of the VTF, but kept  $n$  and  $B_{\theta50}$  constant.

Barring that explanation, we focused on the role of recurrent synapses and disabled the convolution of inputs. We varied the concentration parameters of the synaptic distributions  $\kappa_{inh}$  and  $\kappa_{exc}$  (Figure 7c) in 200 even steps ranging from 0.35 to 7, yielding 40000 possible configurations of the model. This allowed to manipulate the VTF and to accurately reproduce those of single neurons recorded in V1 (neuron A, B in Figure 2b and C in Figure S 1, modeled in Figure 7e). Varying the type of recurrence between neurons with different orientation preference allowed to reproduce all VTF found in V1. The parameter spaces (Figure 7f) showed a trend for resilient VTFs (low  $n$ , high  $B_{\theta50}$ , low  $f_0$ ) to be found mostly around the  $K_{exc} ; K_{inh}$  identity line, thus produced by a balanced recurrent connectivity. Vulnerable VTFs (high  $n$ , low  $B_{\theta50}$ , high  $f_0$ ) were, on the contrary, mostly found above the identity line, where the configuration of the network is dominated by excitation over inhibition. Overall, recurrence within V1 neurons is sufficient to explain the existence of vulnerable and resilient neurons, and thus to explain the co-encoding of orientation and variance.

## Discussion

The variance of oriented inputs to V1 impacts orientation selectivity<sup>9</sup> and we have sought an explanation for how V1 could process this variance, from single neurons to population codes. We have shown that variance causes modulations in tuning (Figure 2) and dynamics (Figure 3) of single V1 neurons, which fall into two broad categories, labeled here vulnerable and resilient (Figure 4). Using a decoding approach, we uncovered variance-dependent accumulative dynamics in the two groups of neurons (Figure 5) that are directly tied to a population-level separation of features within orientation space<sup>28</sup>. Both groups can encode orientation but not variance independently (Figure S 7), yet only resilient neurons are able accurately co-encode orientation and variance of the input to V1 (Figure 6). Based on cortical layer position and on a computational approach (Figure 7), we propose that the overall processing of variance in V1 is performed by recurrent connectivity between local cortical populations with different preferred orientations (Figure 8).

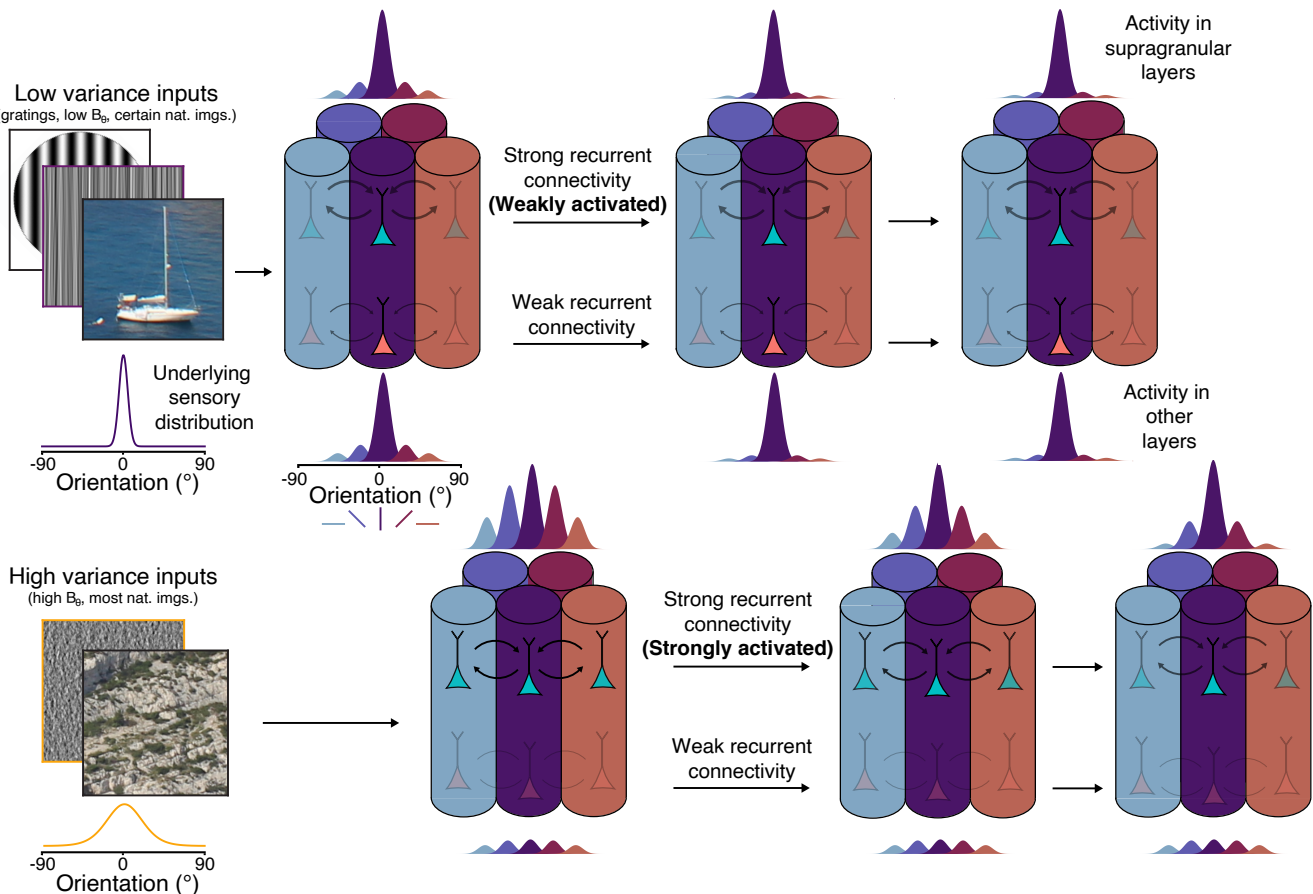


**Figure 8.** Summary of the findings. The top row is a representation of a set of orientation selective units (here, columns) processing low variance inputs, while the bottom row schematizes the processing of high variance inputs. In the case of low variance inputs to V1, the underlying sensory distribution is sharp in the orientation space, driving mostly a single orientation selective unit which processes orientation in fast feedforward manner. The feature encoded by this activity then stays stable through time (from left to right). For inputs of higher orientation variance, the sensory input is broadly distributed in the orientation space, which drives many dissimilarly tuned units, thus recruiting slow recurrent interactions. The quality of feature encoding progressively increases through time, as recurrent interactions perform computations to represent the most salient oriented feature in the input.

213 Here, we restricted our approach to orientation space, rather than investigating the full extent of spatial relationships which  
 214 is present in natural images. As such, full-field stimuli with no second-order correlation were used, which, compared to a  
 215 perfectly ecological environment, have likely excluded end-stopped cells<sup>36</sup>. The time scales reported here might have been  
 216 minimally slowed by anesthesia, here halothane, which nonetheless has a limited effect on V1<sup>37,38</sup>, an area that is also usually  
 217 less prone to anesthetics modulations<sup>39–41</sup>, compared to higher-order areas<sup>42</sup>. Additionally, anesthetized V1 results<sup>43</sup> often  
 218 correlate extremely well with later studies in awake animals<sup>44</sup>.

219 In limiting our approach to orientation space, we also excluded extrastriate contributions to the variance modulations.  
 220 However, there are both neurobiological and computational evidences that V1 alone is sufficient to explain the results, which is  
 221 further supported by the domain literature and by theoretical considerations. In line with our results, recurrent excitatory and  
 222 inhibitory synaptic connectivity is heterogeneous in V1<sup>45–48</sup>, which sustains a resilient orientation tuning<sup>49</sup> that could very well  
 223 account for the diversity of single neurons resilience under different connectivity configuration, as shown by our computational  
 224 model (Figure 7). The temporal scales of local recurrent connectivity, namely the slowly-conducted horizontal waves in an  
 225 orientation map<sup>44</sup>, also fit the view of variance processing as an iterative and accumulative computation implemented by local  
 226 recurrent interactions. Supragranular layers, which contained a majority of resilient neurons, are heavily connected through  
 227 recurrent interactions with neighbouring cortical columns<sup>26,27,32,44</sup>, reinforcing the idea that this type of connectivity could  
 228 explain the different neuronal response to variance. On the computational side, we used a model specifically designed to  
 229 produce intra-V1 data (and here, fitted to cat V1 data<sup>35</sup>) and showed that it is sufficient to produce various VTF as found in our

recordings. This model relies on pooling information from multiple orientation-tuned units into a single neurons, which could also be viewed as a (flattened across recurrence) converging feedforward model. This would be a canonical model of a complex cell, whose computations can be equivalently implemented by a recurrent network<sup>50</sup>. Motion Clouds are however aperiodic patterns and a modulation "F1/F0" ratio cannot be computed here directly.

Investigation of the electrophysiological basis of variance processing are few, but are all in agreement with local V1 processes. For instance, Goris *et al.*<sup>9</sup>, reported that heterogeneously tuned V1 (and also V2) populations help encode the orientation distributions found in natural images, which can be explained by an L-NL model. Consistent with their findings, we reported a variety of single-neuron variance modulations, that serve as a basis to decode orientation variance at the population level — a requirement for encoding natural images in V1<sup>51</sup>. Further analysis of their results has shown a "variance in / variance out" relationship in V1 neurons<sup>17</sup>, which is here implemented in the linear VTF neurons.

Theoretical considerations are also in favor of the claim that intra-V1 recurrence is sufficient to explain variance modulation. Bayesian inference , namely under the specific case of predictive coding<sup>31</sup>, canonically assigns (inverse) variance weighting of cortical activity to supragranular recurrent connectivity<sup>6,8</sup>, without the need for extrastriate computations. This is an interesting perspective which opens up a general interpretation of our results into the broader context of processing variance/precision/uncertainty at different scales of investigations. Extending the present results to other cortical areas or other sensory modalities would be a simple process, given the generative stimulus framework used here<sup>18</sup>, which could yield pivotal new insights into our understanding of predictive processes in the brain.

## Methods

### Visual stimulation

Motion Clouds are generative model-based stimuli<sup>18</sup> which allow for fine parameterized control over a naturalistic stimuli<sup>52</sup>, which is a desirable trait when probing sensory systems under realistic conditions<sup>21</sup>. They are mathematically defined as band-pass filtered white noise stimuli, whose filters in Fourier space are defined as a parameterized distribution in a given perceptual axis (here, only orientation, but can be extended to motion<sup>53</sup> and scale<sup>54</sup>). Thus, the Motion Clouds presently used are fully characterized by their mean orientation and their orientation bandwidth, such that a given stimuli  $S$  can be defined as:

$$S = \mathcal{F}^{-1}(O(\theta, B_\theta)) \quad (1)$$

where  $\mathcal{F}$  is the Fourier transform and  $O$  the orientation envelope, characterized by its mean orientation  $\theta$  and its orientation bandwidth  $B_\theta$ . A total of 96 different stimuli were generated, with 12 mean orientations  $\theta$  ranging from 0 to  $\pi$  in even steps, and 8 orientation bandwidth  $B_\theta$  ranging from  $\approx 0$  to  $\pi/5$  in even steps. The orientation envelope is a von Mises distribution:

$$O(\theta, B_\theta) = \exp \left\{ \frac{\cos(2(\theta_f - \theta))}{4 \cdot B_\theta^2} \right\} \quad (2)$$

where  $\theta_f$  is the angle of the frequency components of the envelope in the Fourier plane, which controls the spatial frequency parameters of the stimuli, set here at 0.9 cycle per degree. The stimuli were drifting orthogonally in either direction with respect to the mean orientation  $\theta$  at a speed of 10°/s, which is optimal to drive V1 neurons<sup>55</sup>. For the range of values of  $B_\theta$  considered here, the orientation envelope approximates a Gaussian distribution and  $B_\theta$  is thus a measure of the variance of the orientation content of the stimuli.

All stimuli were generated using open-source Python code (see Additional information) and displayed using Psychopy<sup>56</sup>. Monocular stimuli were projected with a ProPixed projector (VPixx Technologies Inc.) onto an isoluminant screen (Da-Lite<sup>©</sup>) covering 104°×79° of visual angle. All stimuli were displayed at 100% contrast for 300 ms, interleaved with a mean luminance screen (25 cd/m<sup>2</sup>) shown for 150 ms between each trial. Trials were fully randomized, and each stimulus (a unique combination of  $\theta \times B_\theta \times$  drift direction) was presented 15 times.

### Surgery

Experiments were conducted on 3 adult cats (3.6 - 6.0 kg, 2 males). All surgical and experimental procedures were carried out in compliance with the guidelines of the Canadian Council on Animal care and were approved by the Ethics Committee of the University of Montreal (CDEA #20-006). Animals were initially sedated using acepromazine (Atravet®, 1 mg/kg) supplemented by atropine (0.1 mg/kg). Anesthesia was induced with 3.5% isoflurane in a 50:50 mixture of O<sub>2</sub>:N<sub>2</sub>O (v/v). Following tracheotomy, animals underwent artificial ventilation as paralysis was achieved and maintained with an intravenous injection of 2% gallamine triethiodide (10 mg/kg/h) diluted in a 1:1 (v/v) solution of 5% dextrose lactated ringer solution. Through the experiment, the expired level of CO<sub>2</sub> was maintained between 35 and 40 mmHg by adjusting the tidal volume and respiratory rate. Heart rate was monitored and body temperature was maintained at 37°C by means of a feedback-controlled heated blanket. Lidocaine hydrochloride (2%) was applied locally at all incisions and pressure points and a craniotomy was

277 performed over area 17 (V1) contralaterally to the stimulated eye (Horsley-Clarke coordinates 4-8P; 0.5-2L). Dexamethasone  
 278 (4 mg) was administered intramuscularly every 12h to reduce cortical swelling. Eye lubricant was regularly applied to avoid  
 279 corneal dehydration.

### 280 Electrophysiological recordings

281 During each recording session, pupils were dilated using atropine (Mydriacyl) while nictitating membranes were retracted  
 282 using phenylephrine (Mydrin). Rigid contact lenses of appropriate power were used to correct the eyes' refraction. Anesthesia  
 283 was changed to 0.5-1% halothane to avoid anesthesia-induced modulation of visual responses<sup>38</sup>. Finally, small durectomies  
 284 were performed before each electrode insertion and a 2% agar solution in saline was applied over the exposed cortical  
 285 surface to stabilize recordings. Linear probes ( $\approx 1 \text{ M}\Omega$ , 1x32-6mm-100-177, Neuronexus) were lowered in the cortical tissue  
 286 perpendicularly to the pia and extracellular activity was acquired at 30KHz using an Open Ephys acquisition board<sup>57</sup>. Single  
 287 units were isolated using Kilosort 2<sup>58</sup> and manually curated using Phy<sup>59</sup>. Clusters with low amplitude templates or ill-defined  
 288 margin were excluded from further analysis. Additional exclusion was performed if a cluster's was unstable (firing rate below 5  
 289 spikes.s<sup>-1</sup> for more than 30 seconds), or if the neuron was not deemed sufficiently orientation selective ( $R^2 < 0.75$  when fitted  
 290 with a von Mises distribution). Laminar positions were determined by the depth of the recording site with respect to the pia,  
 291 which was then cross-validated by looking at the evoked Local Field Potential (LFP) using sink/source analysis<sup>60,61</sup>.

### 292 Single neuron analysis

293 Orientation tuning curves were computed by selecting a 300 ms window maximizing spike-count variance<sup>62</sup>. The firing rate  
 294 was averaged across drift directions and a von Mises distribution<sup>63</sup> was fitted to the data:

$$f(\theta_k) = R_0 + (R_{\max} - R_0) \cdot \exp \left\{ \kappa \cdot (\cos(2(\theta_k - \theta_{\text{pref}})) - 1) \right\} \quad (3)$$

295 where  $\theta_k$  is the orientation of the stimuli,  $R_{\max}$  is the response (baseline subtracted) at the preferred orientation  $\theta_{\text{pref}}$ ,  $R_0$  the  
 296 response at the orientation orthogonal to  $\theta_{\text{pref}}$  and  $\kappa$  a measure of concentration. To control for direction selectivity when  
 297 averaging tuning curves across drift direction, we computed a direction selectivity index:

$$D_s = \frac{R_{\text{pref}} - R_{\text{null}}}{R_{\text{pref}}} \quad (4)$$

298 where  $R_{\text{pref}}$  is the firing rate at the preferred direction (baseline subtracted) and  $R_{\text{null}}$  the firing rate at the preferred direction  
 299 plus  $\pi$ . The quality of each tuning curve was assessed by computing a global metric, the circular variance (CV) of the unfitted  
 300 data, which varies from 0 for perfectly orientation-selective neurons to 1 for orientation-untuned neurons<sup>27</sup>. It is defined as:

$$\text{CV} = 1 - \left| \frac{\sum_k R(\theta_k) \exp \{2i\theta_k\}}{\sum_k R(\theta_k)} \right| \quad (5)$$

301 where  $R(\theta_k)$  is the response of a neuron (baseline subtracted) to a stimulus of angle  $\theta_k$ . The changes of CV as a function of  $B_\theta$   
 302 were fitted with a Naka-Rushton function<sup>22</sup>:

$$f(B_\theta) = f_0 + f_{\max} \frac{B_\theta^n}{B_\theta^n + B_{\theta50}^n} \quad (6)$$

303 where  $f_0$  is the base value of the function,  $f_0 + f_{\max}$  its maximal value,  $B_{\theta50}$  the stimulus' variance at half  $f_{\max}$  and  $n$  a strictly  
 304 positive exponent of the function.

305 The significance of the tuning to orientation was measured by comparing the unfitted firing rate at the preferred and  
 306 orthogonal orientations across trials, using a Wilcoxon signed-rank test correct for continuity, and the maximum value of  
 307  $B_\theta$  which yielded a significant result was designed as  $B_{\theta\max}$  (i.e., the maximum variance at which a neuron is still tuned).  
 308 Shifts of the preferred orientation were evaluated as the difference of  $\theta_{\text{pref}}$  between trials where  $B_\theta = 0^\circ$  and  $B_\theta = B_{\theta\max}$ . The  
 309 significance of the variation of peak amplitude of the tuning curve was measured as by comparing the unfitted firing rate at the  
 310 preferred orientation between trials where  $B_\theta = 0^\circ$  and  $B_\theta = B_{\theta\max}$ .

### 311 Population decoding

312 The parameters used to generate Motion Clouds were decoded from the neural recordings using a multinomial logistic regression  
 313 classifier<sup>28</sup>. For a given stimulus, the activity of all the recorded neurons was a vector  $X(t) = [X_1(t) \ X_2(t) \ \dots \ X_{249}(t)]$ ,  
 314 where  $X_i(t)$  is the spike count of neuron  $i$  in a time window  $[t; t + \Delta T]$ . The onset of this window  $t$  was slid from -200 ms to 400  
 315 ms (relative to the stimulation time) in steps of 10 ms while  $\Delta T$  was kept constant at 100 ms. It should be noted that merging  
 316 neural activity across electrodes or experiments is a common procedure<sup>64,65</sup>, which we validated in our data by verifying that

317 the electrode or experiment which yielded the data could not be decoded from the neural activity (Figure S 6). Mathematically,  
 318 the multinomial logistic regression is an extension of the binary logistic regression<sup>28</sup> trained here to classify the spike vector  
 319  $X(t)$  between  $K$  classes. The probability of any such vector to belong to a given class is:

$$P(y = k|X(t)) = \frac{\exp\{\langle \beta_k, X(t) \rangle\}}{\sum_{k'=1}^K \exp\{\langle \beta_{k'}, X(t) \rangle\}} \quad (7)$$

320 where  $\langle \cdot, \cdot \rangle$  is the scalar product over the different neurons,  $k = 1, \dots, K$  is the class out of  $K$  possible values and  $\beta_k$  are the  
 321 coefficients learned during the training procedure of the classifier. Several decoders were trained with classification tasks:  
 322 decoding orientation  $\theta$  ( $K = 12$ , Figure 5), decoding orientation variance  $B_\theta$  ( $K = 8$ , Figure S 7) or both ( $K = 12 \times 8 = 96$ ,  
 323 Figure 6). All meta-parameters (the integration window size, penalty type, regularization strength and train/test split size) were  
 324 controlled, showing that the decoding performances stem mainly from experimental data rather than fine-tuning of the decoder  
 325 parameterization (Figure S 5).

326 The performance of all decoders was reported as the average accuracy across all classes  $K$ , known as the balanced accuracy  
 327 score<sup>66</sup>. The accuracy for each specific class  $k$  can also be reported in the form of a population tuning curve, in which the  
 328 likelihood of decoding each possible class  $K$  is given by equation 7. To estimate the timecourse of the decoders, they were  
 329 fitted in the [0; 300] ms range with a sigmoid function:

$$\sigma = \max_{\text{acc}} \left( \frac{1}{1 + e^{-k\tau}} \right) + \min_{\text{acc}} \quad (8)$$

330 where  $\max_{\text{acc}}$  and  $\min_{\text{acc}}$  are respectively the maximum and minimum accuracies of the decoder,  $k$  the steepness and  $\tau$  the time  
 331 constant of the function.

### 332 Computational model

333 We used a recurrent network of orientation-tuned neurons to model responses to increasing orientation variance  $B_\theta$ . The model  
 334 presently used was first used to account for the intracortical activity in the cat primary visual cortex<sup>33</sup>, although it was presently  
 335 simplified as a center-surround filter in the orientation domain<sup>27</sup>. Notably, this network has been able to account for numerous  
 336 experimental findings, including learning and adaptation of cortical neurons<sup>34,35</sup>, whose implementations are similar to ours.

337 The model consisted of  $N$  orientation-tuned neurons, evenly tiling the orientation space between  $-\pi$  and  $\pi$ . Each neuron is  
 338 modeled as a single passive unit whose membrane potential obeys the equation:

$$\tau \delta V / \delta T + V = V_{\text{ff}} + V_{\text{exc}} - V_{\text{inh}} \quad (9)$$

339 where  $\tau$  is the membrane time constant and  $V_{\text{ff}}$ ,  $V_{\text{exc}}$ ,  $V_{\text{inh}}$  are the synaptic potentials coming from the feedforward input,  
 340 recurrent excitatory and recurrent inhibitory connectivity, respectively. The firing rate  $R$  at time  $t$  of each neuron is computed as  
 341 an instantaneous quantity modulated by a gain  $\alpha$ :

$$R(t) = \alpha \max(V(t), 0) \quad (10)$$

342 For computational simplicity, the neurons had no spontaneous firing rate and  $V$  was measured relative to the firing threshold.  
 343 Each neuron could send mixed excitatory and inhibitory synaptic potentials to its neighbour, although this specific model has  
 344 been reported to achieve similar behaviour with separate units<sup>35</sup>. For each stimulus of main orientation  $\theta$ , the input to a cell  
 345 with preferred orientation  $\theta_{\text{pref}}$  is:

$$V_{\text{ff}}(\theta_{\text{pref}}) = J_{\text{ff}} \frac{e^{\kappa_{\text{ff}} \cos(2(\theta - \theta_{\text{pref}}))}}{2\pi I_0(\kappa_{\text{ff}})} \quad (11)$$

346 where  $J_{\text{ff}}$  is the strength of the input and  $I_0$  is the modified Bessel function of order 0. The right-hand side of the equation  
 347 describes a von Mises with mean  $\theta_{\text{pref}}$  and concentration  $\kappa_{\text{ff}}$ . This latter parameter is related to the orientation bandwidth  $B_\theta$ ,  
 348 which was varied to yield a model's TVF  $B_\theta/CV$  curves:

$$B_\theta = \sqrt{\frac{0.5 \arccos((\log(0.5) + \kappa_{\text{ff}}) / \kappa_{\text{ff}})}{2 \log(2)}} \quad (12)$$

349 a total of 20  $B_\theta$  spanning the same range used in the experiments were used, each with 32 different  $\theta$  tiling a  $[-75^\circ; 75^\circ]$   
 350 orientation space. The recurrent connectivity profile for excitatory ( $C_{\text{exc}}$ ) and inhibitory ( $C_{\text{inh}}$ ) synapses was controlled by  
 351 separate von Mises distributions over the orientation space  $\Theta$ :

$$C_{\text{exc}}(\theta_{\text{pref}}) = \frac{e^{\kappa_{\text{exc}} \cos(2(\Theta - \theta_{\text{pref}}))}}{2\pi I_0(\kappa_{\text{exc}})} \quad (13)$$

$$C_{\text{inh}}(\theta_{\text{pref}}) = \frac{e^{\kappa_{\text{inh}} \cos(2(\theta - \Theta_{\text{pref}}))}}{2\pi I_0(\kappa_{\text{inh}})} \quad (14)$$

353 which are both used to describe an overall connectivity kernel:

$$C_{\text{tot}}(\theta_{\text{pref}}) = J_{\text{exc}} C_{\text{exc}} - J_{\text{inh}} C_{\text{inh}} \quad (15)$$

354 which followed a typical Ricker wavelet (or Mexican hat) shape (Figure 7d). The overall activity of the network is then a  
355 weighted sum of the firing rates of all the neurons:

$$V_{\text{exc}} - V_{\text{inh}}(t) = \sum_{\Theta} C_{\text{tot}}(\theta_{\text{pref}}) R(t) \quad (16)$$

356 Parameterization of the model was done to match single V1 neuron recordings of anesthetized cats, in an experimental setup  
357 similar to the one used here<sup>67</sup>. The computational procedure to match experimental data was entirely done in a previous  
358 publication<sup>35</sup>. Briefly, it consisted in scanning a range of possible values for each parameters, then fine all possible combinations  
359 using a metric of likeliness to single grating response, time-to-peak, peak response and tuning width. The parameters yielded  
360 by this procedure were  $\tau = 10.8$  ms;  $\alpha = 10.6$  Hz/mV;  $J_{\text{ff}} = 9.57$  mv/Hz;  $J_{\text{exc}} = 1.71$  Hz/mV;  $J_{\text{inh}} = 2.0178$  Hz/mV. For the  
361 feedforward mode of the model (Figure 7e),  $J_{\text{exc}}$  and  $J_{\text{inh}}$  were set to 0 Hz/mV and the input was convolved with a "receptive  
362 field" :

$$\text{RF} = \frac{e^{\kappa_{\text{RF}} \cos(2(\theta - \Theta_{\text{pref}}))}}{2\pi I_0(\kappa_{\text{RF}})} \quad (17)$$

363 of which we reported the Half-Width at Half-Height, given by<sup>68</sup> :

$$\text{HWHH} = 0.5 \arccos\left(\frac{\log(0.5) + \kappa}{\kappa}\right) \quad (18)$$

364 For the recurrent mode (Figure 7f-h), the concentration measures of the recurrent connectivity profiles  $\kappa_{\text{exc}}$  and  $\kappa_{\text{inh}}$  were  
365 both varied from 0.35 to 7, in 200 even steps, and the input was not convolved with a receptive field.

### 366 Statistical procedures and plotting

367 All data was analyzed using custom Python code (see Additional information). Statistical analysis was performed using non-  
368 parametric tests. Wilcoxon signed-rank test with discarding of zero-differences was used for paired samples and Mann-Whitney  
369 U test with exact computation of the  $U$  distribution was used for independent samples. Due to the impracticality of using error  
370 bars when plotting time series, colored contours are used to represent standard deviation values (unless specified otherwise),  
371 with a solid line representing mean values. For boxplots, the box extends from the lower to upper quartile values, with a solid  
372 white line at the median value. The upper and lower whiskers extend to respectively  $Q1 - 1.5 * IQR$  and  $Q3 + 1.5 * IQR$ , where  
373  $Q1$  and  $Q3$  are the lower and upper quartiles and  $IQR$  is the inter-quartile range.

### 374 Data availability

375 Data and analysis code that have been used in the present study can be made available from the corresponding author upon  
376 reasonable request.

### 377 References

- 378 1. Hubel, D. H. & Wiesel, T. N. Receptive fields of single neurones in the cat's striate cortex. *The J. physiology* **148**, 574  
379 (1959).
- 380 2. Priebe, N. J. Mechanisms of orientation selectivity in the primary visual cortex. *Annu. review vision science* **2**, 85–107  
381 (2016).
- 382 3. Fiser, J., Chiu, C. & Weliky, M. Small modulation of ongoing cortical dynamics by sensory input during natural vision.  
383 *Nature* **431**, 573–578 (2004).
- 384 4. Simoncelli, E. P. & Olshausen, B. A. Natural image statistics and neural representation. *Annu. review neuroscience* **24**,  
385 1193–1216 (2001).

- 386 5. Helmholtz, H. v. *Treatise on physiological optics, 3 vols.* (Optical Society of America, 1924).
- 387 6. Friston, K. A theory of cortical responses. *Philos. transactions Royal Soc. B: Biol. sciences* **360**, 815–836 (2005).
- 388 7. Barthélémy, S. & Mamassian, P. Evaluation of objective uncertainty in the visual system. *PLoS computational biology* **5**, e1000504 (2009).
- 390 8. Bastos, A. M. *et al.* Canonical microcircuits for predictive coding. *Neuron* **76**, 695–711 (2012).
- 391 9. Goris, R. L., Simoncelli, E. P. & Movshon, J. A. Origin and function of tuning diversity in macaque visual cortex. *Neuron* **88**, 819–831 (2015).
- 393 10. Orbán, G., Berkes, P., Fiser, J. & Lengyel, M. Neural variability and sampling-based probabilistic representations in the  
394 visual cortex. *Neuron* **92**, 530–543 (2016).
- 395 11. Festa, D., Aschner, A., Davila, A., Kohn, A. & Coen-Cagli, R. Neuronal variability reflects probabilistic inference tuned to  
396 natural image statistics. *Nat. communications* **12**, 1–11 (2021).
- 397 12. Keeble, D., Kingdom, F., Moulden, B. & Morgan, M. Detection of orientationally multimodal textures. *Vis. Res.* **35**,  
398 1991–2005 (1995).
- 399 13. Beaudot, W. H. & Mullen, K. T. Orientation discrimination in human vision: Psychophysics and modeling. *Vis. research*  
400 **46**, 26–46 (2006).
- 401 14. Phillips, G. C. & Wilson, H. R. Orientation bandwidths of spatial mechanisms measured by masking. *JOSA A* **1**, 226–232  
402 (1984).
- 403 15. Heeley, D., Timney, B., Paterson, I. & Thompson, R. Width discrimination for band-pass stimuli. *Vis. research* **29**, 901–905  
404 (1989).
- 405 16. Heeley, D. W. & Buchanan-Smith, H. M. The influence of stimulus shape on orientation acuity. *Exp. Brain Res.* **120**,  
406 217–222 (1998).
- 407 17. Hénaff, O. J., Boundy-Singer, Z. M., Meding, K., Ziemba, C. M. & Goris, R. L. Representation of visual uncertainty  
408 through neural gain variability. *Nat. communications* **11**, 1–12 (2020).
- 409 18. Leon, P. S., Vanzetta, I., Masson, G. S. & Perrinet, L. U. Motion clouds: model-based stimulus synthesis of natural-like  
410 random textures for the study of motion perception. *J. neurophysiology* **107**, 3217–3226 (2012).
- 411 19. Johnson, A. P. & Baker, C. L. First-and second-order information in natural images: a filter-based approach to image  
412 statistics. *JOSA A* **21**, 913–925 (2004).
- 413 20. Field, D. J. Relations between the statistics of natural images and the response properties of cortical cells. *Josa a* **4**,  
414 2379–2394 (1987).
- 415 21. Rust, N. C. & Movshon, J. A. In praise of artifice. *Nat. neuroscience* **8**, 1647–1650 (2005).
- 416 22. Naka, K. & Rushton, W. A. S-potentials from colour units in the retina of fish (cyprinidae). *The J. physiology* **185**, 536–555  
417 (1966).
- 418 23. Thorndike, R. L. Who belongs in the family. In *Psychometrika* (Citeseer, 1953).
- 419 24. Laughlin, S. A simple coding procedure enhances a neuron's information capacity. *Zeitschrift für Naturforschung c* **36**,  
420 910–912 (1981).
- 421 25. Kinouchi, O. & Copelli, M. Optimal dynamical range of excitable networks at criticality. *Nat. physics* **2**, 348–351 (2006).
- 422 26. Ringach, D. L., Hawken, M. J. & Shapley, R. Dynamics of orientation tuning in macaque primary visual cortex. *Nature*  
423 **387**, 281–284 (1997).
- 424 27. Ringach, D. L., Shapley, R. M. & Hawken, M. J. Orientation selectivity in macaque V1: diversity and laminar dependence.  
425 *J. Neurosci.* **22**, 5639–5651 (2002).
- 426 28. Bishop, C. M. *Pattern recognition and machine learning* (springer, 2006).
- 427 29. Berens, P. *et al.* A fast and simple population code for orientation in primate V1. *J. Neurosci.* **32**, 10618–10626 (2012).
- 428 30. Roelfsema, P. R., Engel, A. K., König, P. & Singer, W. Visuomotor integration is associated with zero time-lag synchronization among cortical areas. *Nature* **385**, 157–161 (1997).
- 429 31. Aitchison, L. & Lengyel, M. With or without you: predictive coding and bayesian inference in the brain. *Curr. opinion  
neurobiology* **46**, 219–227 (2017).

- 432 32. Douglas, R. J., Martin, K. A. & Whitteridge, D. A canonical microcircuit for neocortex. *Neural computation* **1**, 480–488  
433 (1989).
- 434 33. Somers, D. C., Nelson, S. B. & Sur, M. An emergent model of orientation selectivity in cat visual cortical simple cells. *J.  
435 neuroscience* **15**, 5448–5465 (1995).
- 436 34. Teich, A. F. & Qian, N. Learning and adaptation in a recurrent model of v1 orientation selectivity. *J. Neurophysiol.* **89**,  
437 2086–2100 (2003).
- 438 35. del Mar Quiroga, M., Morris, A. P. & Krekelberg, B. Adaptation without plasticity. *Cell reports* **17**, 58–68 (2016).
- 439 36. Hubel, D. H. & Wiesel, T. N. Receptive fields and functional architecture in two nonstriate visual areas (18 and 19) of the  
440 cat. *J. neurophysiology* **28**, 229–289 (1965).
- 441 37. Uhl, R. R., Squires, K. C., Bruce, D. L. & Starr, A. Effect of halothane anesthesia on the human cortical visual evoked  
442 response. *Anesthesiology* **53**, 273–276 (1980).
- 443 38. Villeneuve, M. Y. & Casanova, C. On the use of isoflurane versus halothane in the study of visual response properties of  
444 single cells in the primary visual cortex. *J. neuroscience methods* **129**, 19–31 (2003).
- 445 39. Martinez-Conde, S. *et al.* Effects of feedback projections from area 18 layers 2/3 to area 17 layers 2/3 in the cat visual  
446 cortex. *J. Neurophysiol.* **82**, 2667–2675 (1999).
- 447 40. Wang, C., Waleszczyk, W., Burke, W. & Dreher, B. Modulatory influence of feedback projections from area 21a on  
448 neuronal activities in striate cortex of the cat. *Cereb. Cortex* **10**, 1217–1232 (2000).
- 449 41. Huang, L., Chen, X. & Shou, T. Spatial frequency-dependent feedback of visual cortical area 21a modulating functional  
450 orientation column maps in areas 17 and 18 of the cat. *Brain research* **998**, 194–201 (2004).
- 451 42. Hudetz, A. G., Vizuete, J. A., Pillay, S. & Mashour, G. A. Repertoire of mesoscopic cortical activity is not reduced during  
452 anesthesia. *Neuroscience* **339**, 402–417 (2016).
- 453 43. Bringuier, V., Chavane, F., Glaeser, L. & Frégnac, Y. Horizontal propagation of visual activity in the synaptic integration  
454 field of area 17 neurons. *Science* **283**, 695–699 (1999).
- 455 44. Chavane, F. *et al.* Lateral spread of orientation selectivity in v1 is controlled by intracortical cooperativity. *Front. systems  
456 neuroscience* **5**, 4 (2011).
- 457 45. Jia, H., Rochefort, N. L., Chen, X. & Konnerth, A. Dendritic organization of sensory input to cortical neurons in vivo.  
458 *Nature* **464**, 1307–1312 (2010).
- 459 46. Chen, X., Leischner, U., Rochefort, N. L., Nelken, I. & Konnerth, A. Functional mapping of single spines in cortical  
460 neurons in vivo. *Nature* **475**, 501–505 (2011).
- 461 47. Iacaruso, M. F., Gasler, I. T. & Hofer, S. B. Synaptic organization of visual space in primary visual cortex. *Nature* **547**,  
462 449–452 (2017).
- 463 48. Scholl, B., Wilson, D. E. & Fitzpatrick, D. Local order within global disorder: synaptic architecture of visual space.  
464 *Neuron* **96**, 1127–1138 (2017).
- 465 49. Monier, C., Chavane, F., Baudot, P., Graham, L. J. & Frégnac, Y. Orientation and direction selectivity of synaptic inputs in  
466 visual cortical neurons: a diversity of combinations produces spike tuning. *Neuron* **37**, 663–680 (2003).
- 467 50. Chance, F. S., Nelson, S. B. & Abbott, L. F. Complex cells as cortically amplified simple cells. *Nat. neuroscience* **2**,  
468 277–282 (1999).
- 469 51. Olshausen, B. A. & Field, D. J. Emergence of simple-cell receptive field properties by learning a sparse code for natural  
470 images. *Nature* **381**, 607–609 (1996).
- 471 52. Vacher, J., Meso, A. I., Perrinet, L. U. & Peyré, G. Biologically inspired dynamic textures for probing motion perception.  
472 *Adv. neural information processing systems* **28** (2015).
- 473 53. Simoncini, C., Perrinet, L. U., Montagnini, A., Mamassian, P. & Masson, G. S. More is not always better: adaptive gain  
474 control explains dissociation between perception and action. *Nat. neuroscience* **15**, 1596–1603 (2012).
- 475 54. Ravello, C. R., Perrinet, L. U., Escobar, M.-J. & Palacios, A. G. Speed-selectivity in retinal ganglion cells is sharpened by  
476 broad spatial frequency, naturalistic stimuli. *Sci. reports* **9**, 1–16 (2019).
- 477 55. Movshon, J. A., Thompson, I. & Tolhurst, D. Spatial and temporal contrast sensitivity of neurones in areas 17 and 18 of  
478 the cat's visual cortex. *The J. physiology* **283**, 101–120 (1978).
- 479 56. Peirce, J. *et al.* Psychopy2: Experiments in behavior made easy. *Behav. research methods* **51**, 195–203 (2019).

- 480 57. Siegle, J. H. *et al.* Open ephys: an open-source, plugin-based platform for multichannel electrophysiology. *J. neural*  
481 *engineering* **14**, 045003 (2017).
- 482 58. Pachitariu, M., Steinmetz, N. A., Kadir, S. N., Carandini, M. & Harris, K. D. Fast and accurate spike sorting of high-channel  
483 count probes with kilosort. In *Advances in neural information processing systems*, 4448–4456 (2016).
- 484 59. Rossant, C. *et al.* Spike sorting for large, dense electrode arrays. *Nat. neuroscience* **19**, 634–641 (2016).
- 485 60. Katzner, S. *et al.* Local origin of field potentials in visual cortex. *Neuron* **61**, 35–41 (2009).
- 486 61. Maier, A., Adams, G. K., Aura, C. & Leopold, D. A. Distinct superficial and deep laminar domains of activity in the visual  
487 cortex during rest and stimulation. *Front. systems neuroscience* **4**, 31 (2010).
- 488 62. Smith, M. A., Majaj, N. J. & Movshon, J. A. Dynamics of motion signaling by neurons in macaque area mt. *Nat.*  
489 *neuroscience* **8**, 220–228 (2005).
- 490 63. Swindale, N. V. Orientation tuning curves: empirical description and estimation of parameters. *Biol. cybernetics* **78**, 45–56  
491 (1998).
- 492 64. Quiroga, R. Q., Reddy, L., Koch, C. & Fried, I. Decoding visual inputs from multiple neurons in the human temporal lobe.  
493 *J. neurophysiology* **98**, 1997–2007 (2007).
- 494 65. Guitchounts, G., Masis, J., Wolff, S. B. & Cox, D. Encoding of 3d head orienting movements in the primary visual cortex.  
495 *Neuron* **108**, 512–525 (2020).
- 496 66. Brodersen, K. H., Ong, C. S., Stephan, K. E. & Buhmann, J. M. The balanced accuracy and its posterior distribution. In  
497 *2010 20th International Conference on Pattern Recognition*, 3121–3124 (IEEE, 2010).
- 498 67. Felsen, G. *et al.* Dynamic modification of cortical orientation tuning mediated by recurrent connections. *Neuron* **36**,  
499 945–954 (2002).
- 500 68. Swindale, N. V., Grinvald, A. & Shmuel, A. The spatial pattern of response magnitude and selectivity for orientation and  
501 direction in cat visual cortex. *Cereb. cortex* **13**, 225–238 (2003).

## 502 Acknowledgements

503 The authors would like to thank Genevieve Cyr for her technical assistance, Bruno Oliveira Ferreira de Souza and Visou Ady  
504 for experimental advices, Louis Eparvier, Jean-Nicolas Jérémie and Salvatore Giancani for their comments on the manuscript  
505 and Jonathan Vacher for fruitful exchanges on the formalization of the generation of synthetic images and for his contributions  
506 to related analysis of other neurophysiological recordings. This work was supported by ANR project “Horizontal-V1”  
507 ANR-17-CE37-0006 to L.U.P, a CIHR grant to C.C (PJT-148959) and an École Doctorale 62 PhD grant to H.J.L.

## 508 Author contributions

509 L.U.P., C.C. F.C., N.C., and H.J.L. designed the study. H.J.L., N.C. and L.K. collected the data. H.J.L. and L.U.P. analyzed the  
510 data. H.J.L. and L.U.P. wrote the original draft of the manuscript. All authors reviewed and edited the manuscript.

## 511 Competing interests

512 The authors declare no competing interests.

513 **Supplementary information**

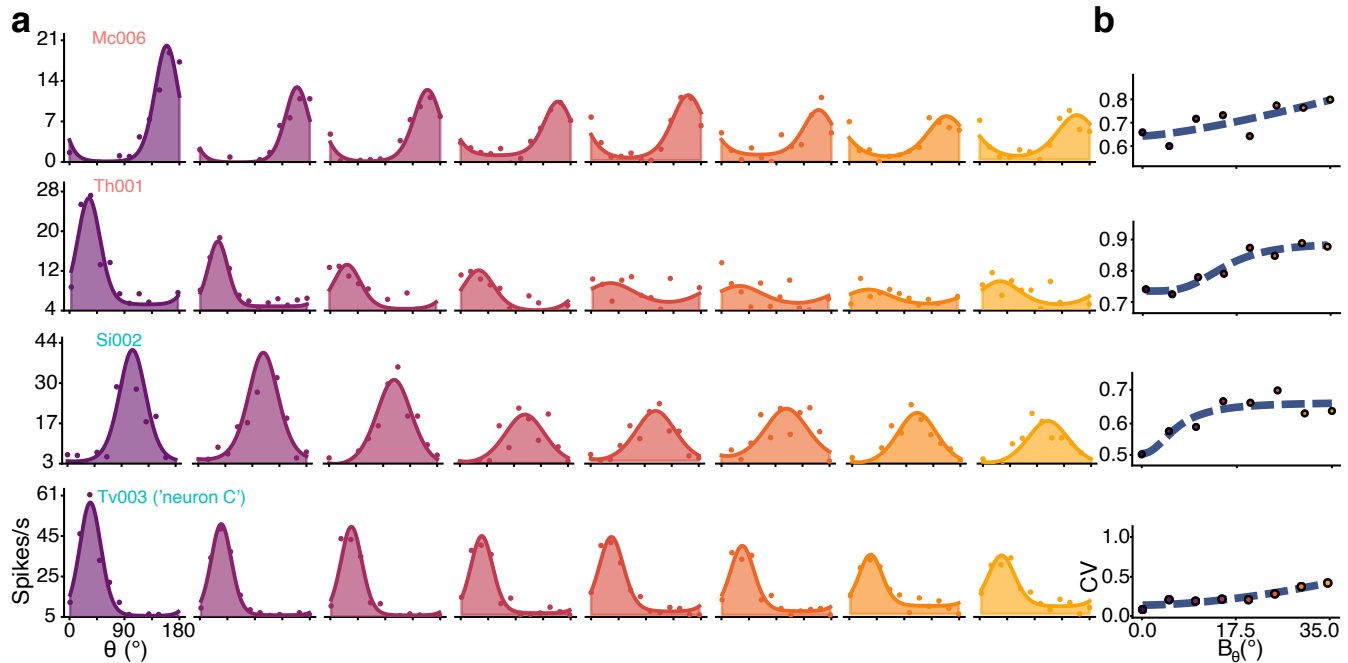


**Figure S 1.** Additional examples of single neuron tuning curves and VTF. **(a)** Tuning curves of four more neurons, stimulated with Motion Clouds of increasing variance  $B_{\theta}$  from left to right. Colored dots represent the mean firing rate across trials (baseline subtracted, 300 ms average) and solid line a fitted von Mises function. **(b)** Variance-tuning functions (VTF), measuring the changes of orientation tuning measured by the circular variance (CV, colored dots) as a function of Motion clouds variance  $B_{\theta}$ , fitted with a Naka-Rushton (NKR) function (dashed curves, parameters shown in light gray).

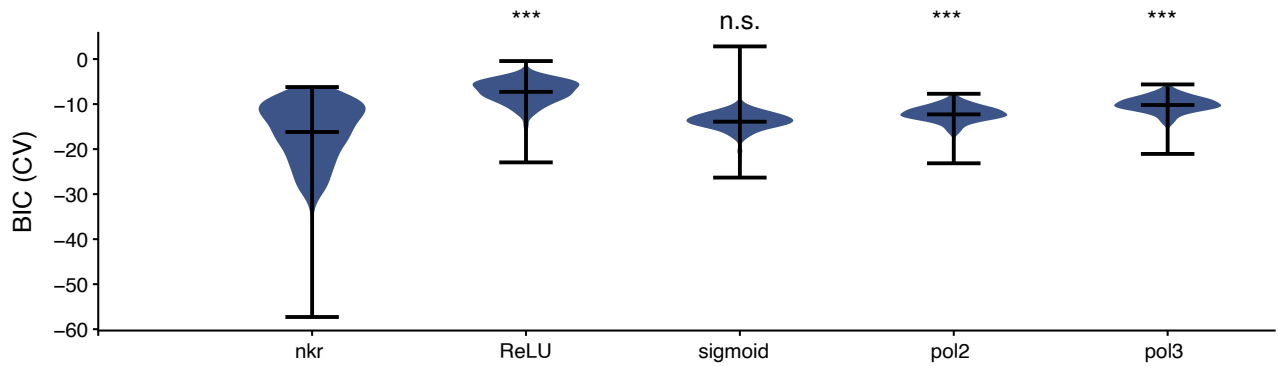


**Figure S 2.** Naka-Rushton functions are the most adequate fit for PRFs. Violin plot of the Bayesian Information Criterion (BIC) of the CV curves of all recorded neurons. Each violin plot represents a different type of fitted equation, respectively: Naka-Rushton (nkr, see Methods) ; Rectified Linear Unit (ReLU,  $f(x) = \max(0, x)$ ) ; logistic function (sigmoid,  $f(x) = \frac{e^x}{e^x + 1}$ ) ; second degree polynomial function (pol2,  $f(x) = ax^2 + bx + c$ ) and third degree polynomial function (pol3,  $f(x) = ax^3 + bx^2 + cx + d$ ). A lower BIC indicates less information lost in the fitting process, hence a better fitting model. Naka-Rushton curves were chosen over sigmoid functions for the skewness of the BIC distributions towards negative values, as well as the explainability of their parameters. n.s., not significant; \*,  $p < 0.05$ ; \*\*,  $p < 0.01$ ; \*\*\*,  $p < 0.001$  (Kruskal-Wallis H-test, post-hoc Dunn Pairwise test, Bonferroni corrected).

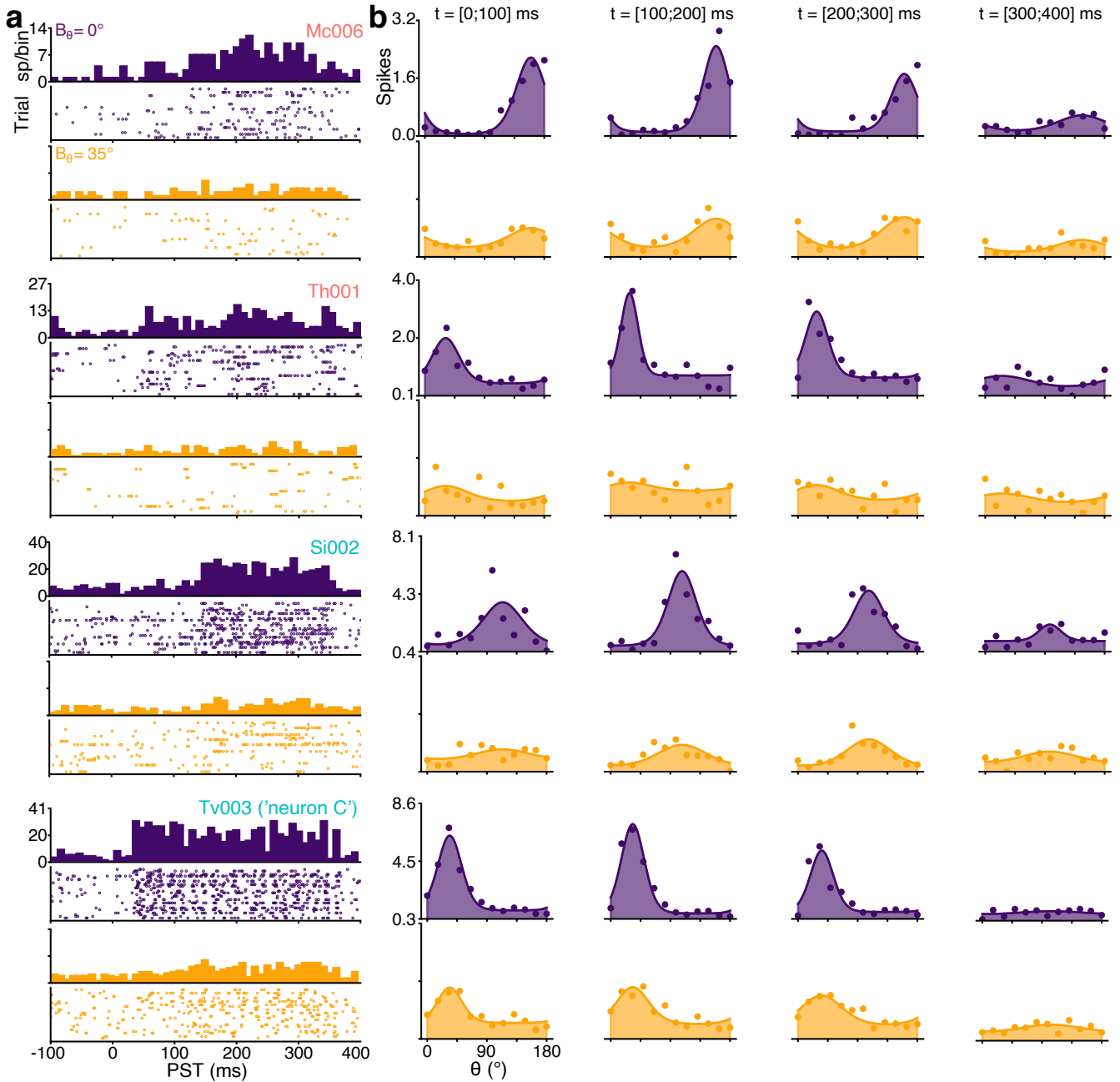


**Figure S 3.** Additional examples of dynamical properties of neurons. **(a)** Peristimulus time (PST) histogram and associated rasterplot of the four additional example neurons, for Motion Clouds with lowest ( $B_\theta = 0^\circ$ , purple) and highest ( $B_\theta = 35^\circ$ , yellow) variance. **(b)** Dynamics of the tuning curves shown in Figure 2 in 100 ms windows, starting at the time labelled atop of each column..

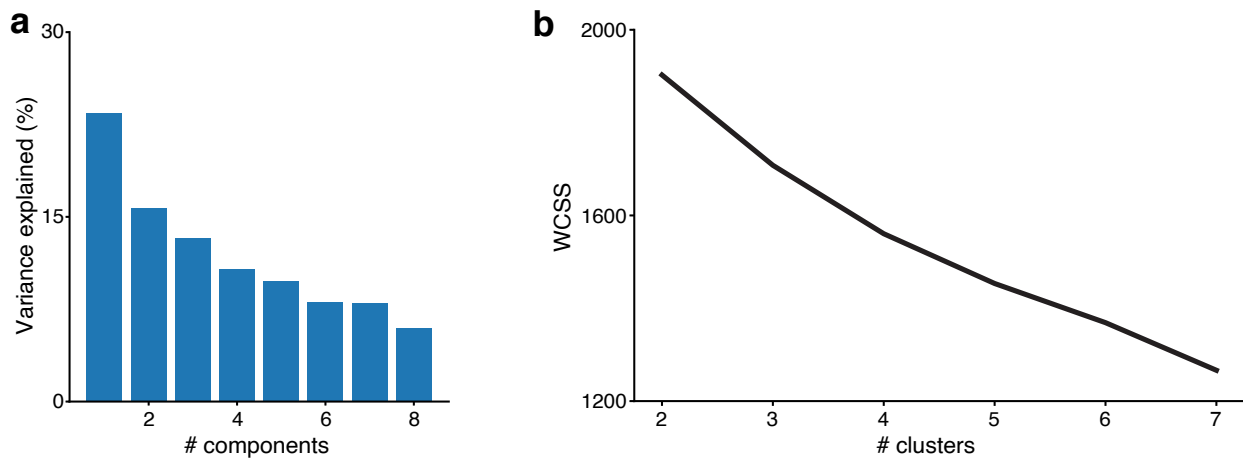


**Figure S 4.** Graphical reports of clustering analysis. **(a)** Fraction of variance explained as a function of the number of components used in the Principal Component Analysis. **(b)** Within-Cluster-Sum-of-Squares (WCSS) of the K-means clustering, expressed as a function of the number of clusters. An empirical way to select the number of clusters is to typically take the "elbow" of such a curve, if existent.

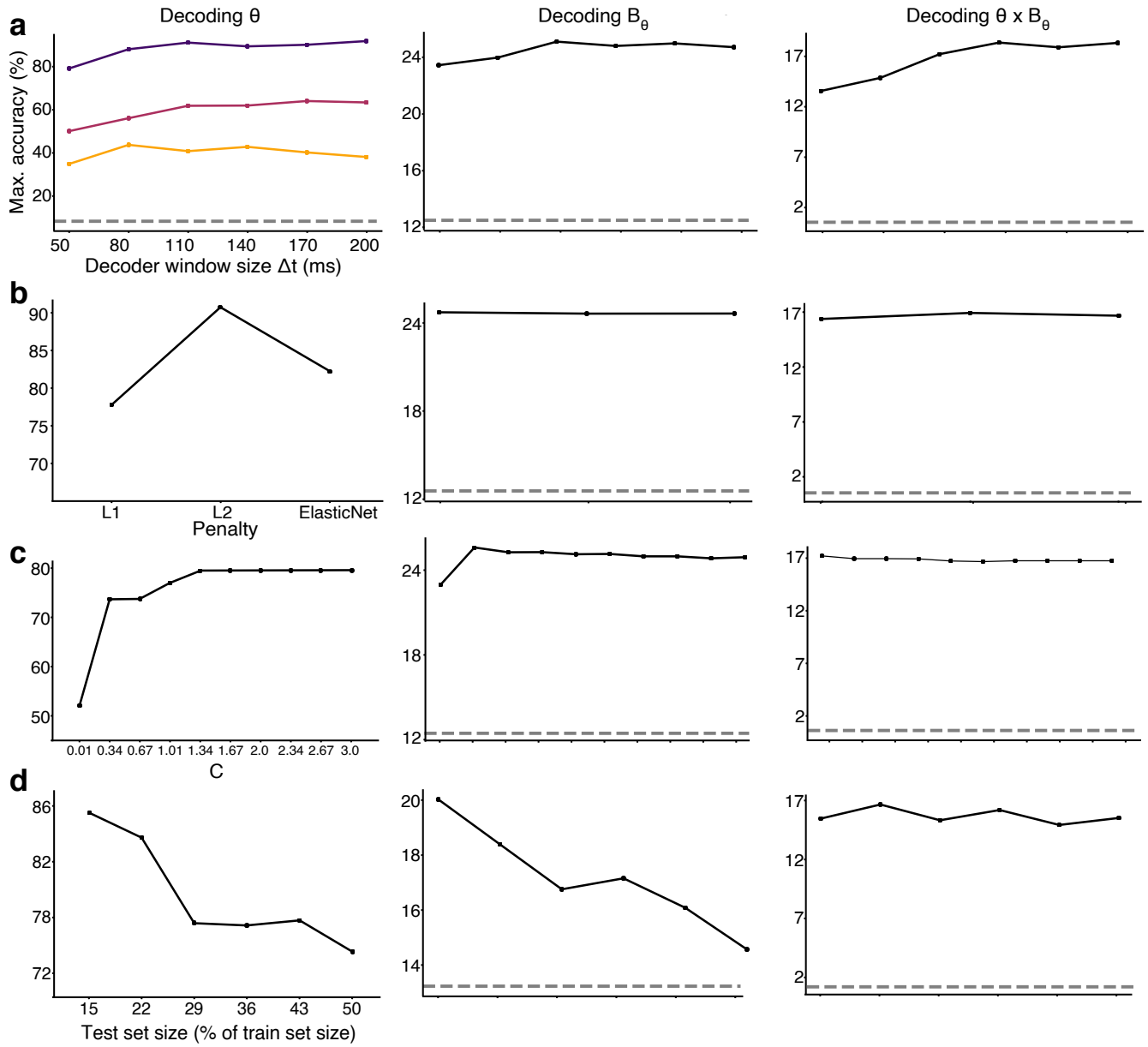


**Figure S 5.** Parameters evaluation of the decoders. **(a)** Parameter scanning of the orientation  $\theta$  decoders for three  $B_\theta$  (chance level 1/12). Maximum accuracy reached during the time course of each decoder is reported for each parameter. On the first row, the parameter optimized is the length of the time window  $\Delta T$ , which controls the length of the integration time of the decoder (see Methods). On the second row, the type of penalization norm applied to the decoder, which controls the metric by which the classification error is minimized.  $l_1$  and  $l_2$  are defined as  $\sum_i |x_i|$  and  $\sqrt{\sum_i |x_i|^2}$ , where  $x$  is a set of features fed to the classifier. The penalization norm "ElasticNet" linearly combines both these norms, here with an equal weighting applied to both norm. On the third row, the parameter  $C$  controls the regularization strength, which measure the magnitude of the penalty applied to large parameters, in order to prevent overfitting on reduced sets of data. On the fourth and last row, we optimized the percentage of data kept out of the training set to evaluate the decoder's accuracy. **(b)** Parameters of the orientation variance  $B_\theta$  decoder (chance level 1/8). **(c)** Parameters of the orientation and orientation variance  $B_\theta \times \theta$  decoder (chance level 1/96).

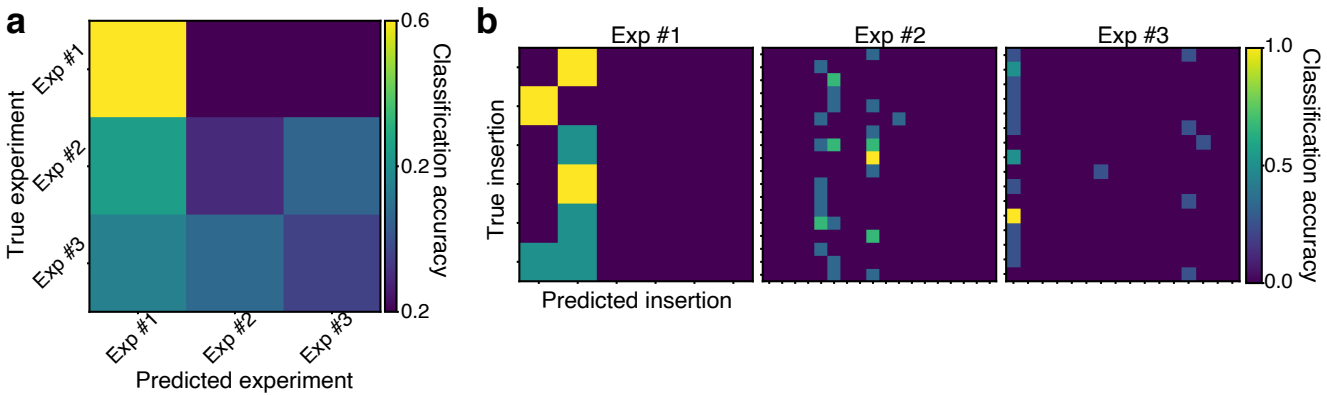


**Figure S 6.** The experiment identity (the specific experiment which yielded the spikes) and insertion identity (the specific insertion which yielded the spikes) of neurons does not produce any significant result, thereby validating the fusion of multiple datasets in the decoding process. **(a)** Confusion matrix of a decoder trained to retrieve the experiment identity using three groups of 30 neurons (bootstrapped 1000 times). **(b)** Confusion matrices of three decoders trained to retrieve the insertion identity of the neurons recorded in each experiment.

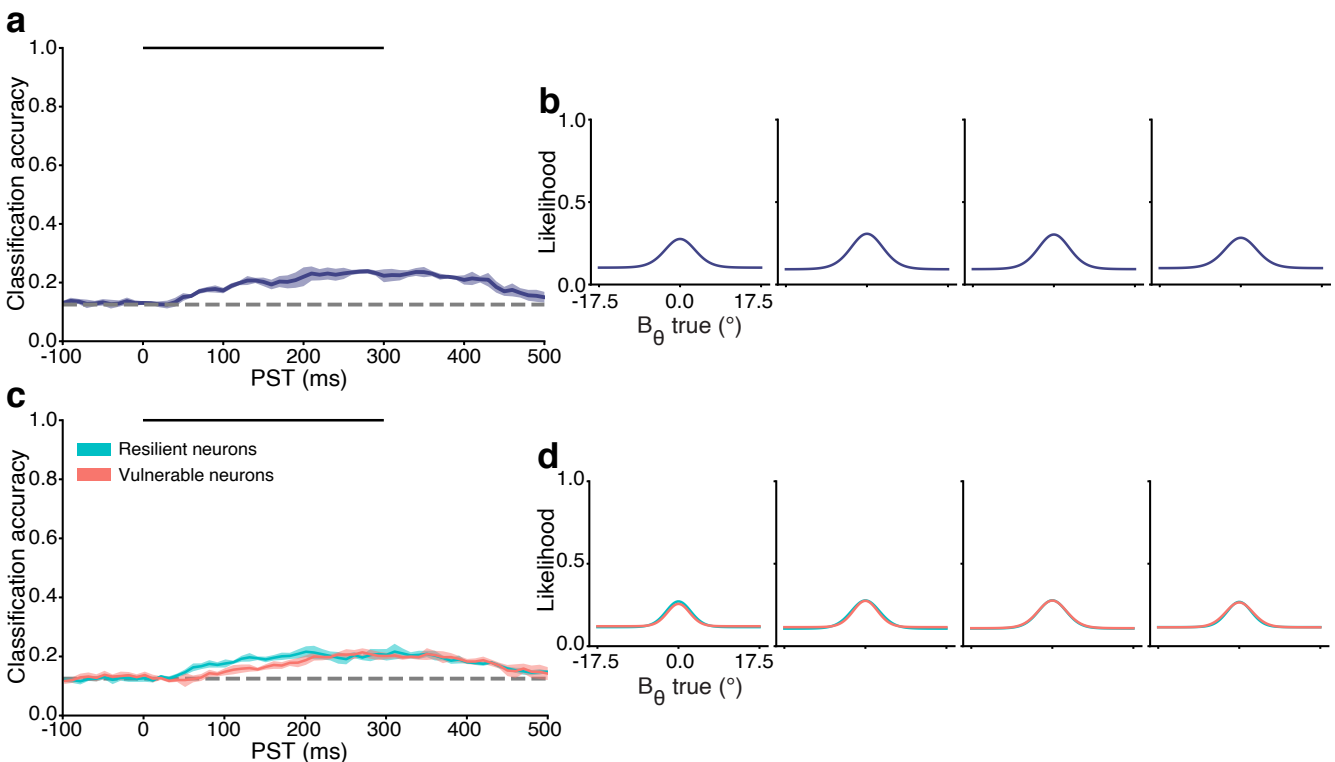


**Figure S 7.** Orientation variance cannot be accurately decoded from the population activity. **(a)** Time course of a decoder trained to retrieve the variance  $B_\theta$  of Motion Clouds. Solid dark line represents the mean accuracy of a 5-fold cross validation and filled contour the SD. Decoding at chance level (here, 1/8) is represented by a gray dashed line. **(b)** Population tuning curve of the decoder. **(c)** Same as Figure S7a, trained with spikes from either resilient or vulnerable neurons. **(d)** Same as Figure S7b, trained with spikes from either resilient or vulnerable neurons.

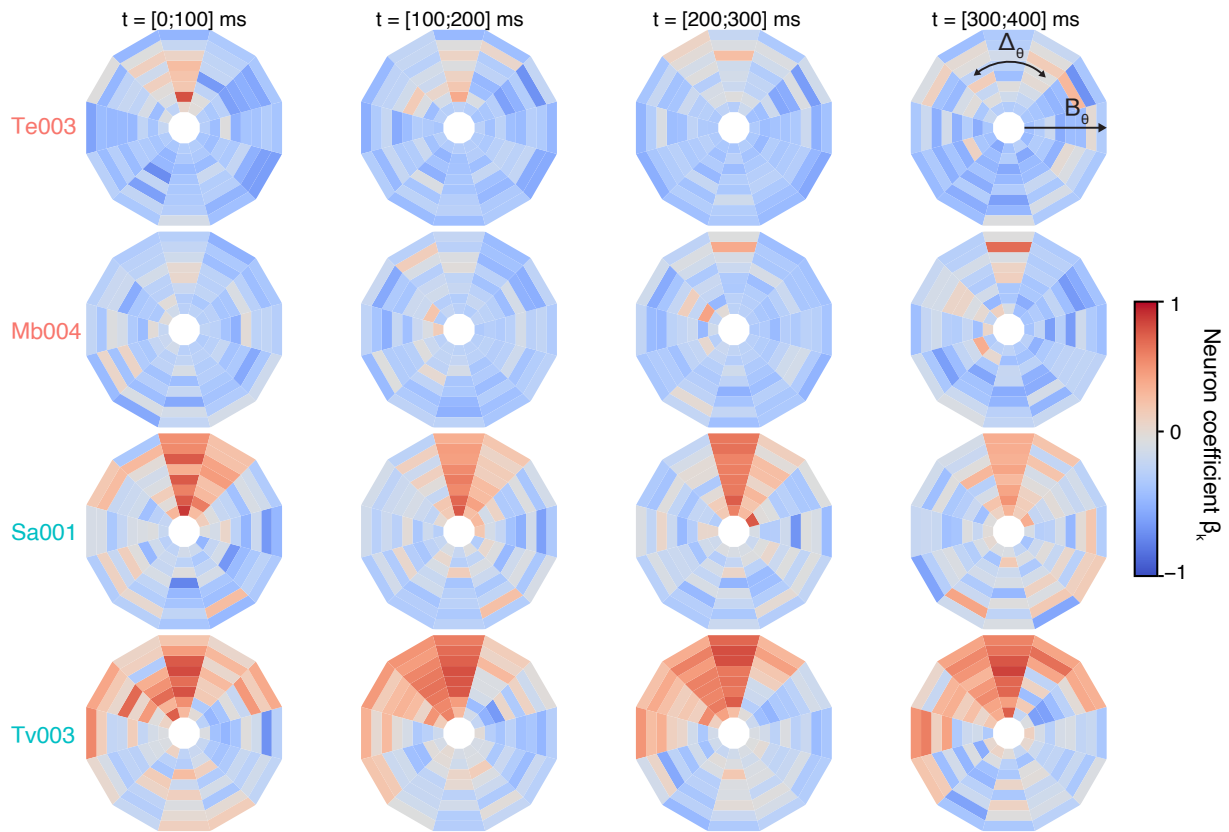


**Figure S 8.** Polar plot of coefficient matrices from two single vulnerable neurons (top rows) and two single resilient neurons (bottom rows). As in Figure 6e, the angle of each bin represents the error on the  $\theta$  identity of the stimulus,  $\Delta_\theta$ , and the eccentricity corresponds to the coefficient for each  $B_\theta$  (highest variance at the edge). The temporal evolution of the coefficients from the decoder is normalized for each neuron by row.